

1 **An object-based approach to differentiate pores and**
2 **microfractures in petrographic analysis using**
3 **explainable, supervised machine learning**

4 **Issac Sujay Anand John Jayachandran^{1,2}, Holly Catherine Gibbs^{3,4}, Juan**
5 **Carlos Laya¹, Yemna Qaiser², Talha Khan², Mohammed Ishaq Mohammed**
6 **Shoeb Ansari⁵, Mohammed Yaqoob Ansari⁵, Mohammed Malyah², Nayef**
7 **Alyafei², Thomas Daniel Seers^{1,2}**

8 ¹Department of Geology & Geophysics, Texas A&M University, College Station, TX 77843, USA

9 ²Department of Petroleum Engineering, Texas A&M University Qatar, Education City, Doha, Qatar

10 ³Department of Biomedical Engineering, Texas A&M University, College Station, TX 77843, USA

11 ⁴Microscopy and Imaging Center, Texas A&M University, College Station, TX 77843, USA

12 ⁵Department of Electrical & Computer Engineering, Texas A&M University at Qatar, Education City,
13 Doha, Qatar

14 **Key Points:**

- 15 • The first study to propose a binary framing for machine learning driven petrographic
16 pore typing
- 17 • Linear and non-linear models perform equally well for idealized microfractures and
18 pores
- 19 • We highlight the need for greater scrutiny in AI models for petrographic pore typ-
20 ing

Corresponding author: Issac Sujay Anand John Jayachandran, sujay92@tamu.edu

Abstract

Petrographic observations are vital for carbonate pore-typing, linking geological frameworks to petrophysical behavior. However, current petrographic pore typing is manual, with the qualitative to semi-quantitative results not easily fitted into quantitative subsurface characterization. Some recent studies have automated this process using supervised machine learning and deep learning, focusing on simple pore morphological features, and have reported high classification accuracies for several complex pore types. However, there are concerns about the validity of these studies due to conceptual and technical flaws in their collective approach. This study was aimed at a more fundamental problem, classifying between open microfractures and open pores in petrographic thin sections using an object-based approach and explainable supervised machine learning. We analyzed 18 carbonate thin-sections from the USA, numerically representing them using five shape features: compactness, aspect ratio, extent, solidity, and formfactor. Using a labeled dataset of 400 microfractures and 400 pores, we evaluated nine of the most widely used supervised models. All models showed high testing accuracies (89.58 - 90.42%). Interestingly, complex non-linear models did not significantly outperform simpler linear ones. Compactness and aspect ratio were the most informative features. However, the labeled datasets did not reflect the overall dataset's complexity, which suggested that high accuracies in similar studies might be due to curated datasets rather than accounting for the true complexity of carbonate pore systems. The study concludes that simple shape features are ineffective for classifying carbonate pore types. It is hoped that this study will provide a foundation for more robust AI-assisted pore typing.

Plain Language Summary

Carbonate pore-typing is a critical task for determining rock types. Petrographic pore typing from thin sections is the most mature form of carbonate pore-typing and is vital in relating the geology of the studied formations to its petrophysical properties. To date, this process has remained manual, bound by human limitations, and difficult to link to quantitative digital reservoir models. Recent research has tried to automate petrographic pore-typing using machine learning and deep learning, claiming very high accuracies. However, there are concerns about these claims due to potential flaws in the methods used. There is potential in using machine learning for binary classification, especially when distinguishing between microfractures and pores, as they are quite distinct in shape. In this study we used an object-based, supervised machine learning approach to differentiate these two classes, using data from 18 carbonate thin sections sourced from the USA. The data was represented using five popular shape features: namely, compactness, aspect ratio, extent, solidity, and formfactor. We used nine popular linear and non-linear supervised machine learning models. The machine learning models tested had an accuracy of around 90 percent. Interestingly, the more complex non-linear models didn't perform much better than simpler, linear models, suggesting that distinguishing between microfractures and pores might be a straightforward problem. Among the shape features, compactness and aspect ratio proved the most useful in separating the two classes. However, we also report that the labeled dataset used for training the models did not represent the full dataset well, thus indicating that simple shape features cannot accurately capture the complexity of carbonate pore types even at the base binary level. The study concludes that while machine learning is promising for simplistic datasets, we must consider more complex shape features and build larger datasets to develop deep learning models. The hope is that this research will guide future efforts in machine-learning and deep-learning approaches to carbonate pore-type classification.

69 **1 Introduction**

70 Pore classification in carbonate lithologies is a fundamental requirement for sub-
 71 surface characterization workflows, serving application areas such as carbon capture, uti-
 72 lization, and storage, and hydrocarbon extraction, among others. Critically, carbonate
 73 pore-typing serves as the bridge between the geological framework of the subsurface and
 74 its petrophysical behavior and is therefore vital to assessing reservoir/aquifer quality (Lønøy,
 75 2006); (Skalinski & Kenter, 2015). Since carbonate pore systems encompass a wide range
 76 of scales (nanometric to kilometeric scales), holistic pore-typing requires the integration
 77 of visual petrographic observations at the thin-section scale with petrophysical data from
 78 core plugs and/or well-logs (Skalinski & Kenter, 2015). In this study, we focus on visual
 79 petrographic pore-typing, which of the aforementioned data types presents the most direct
 80 link to the sedimentological and diagenetic framework of the reservoir and repre-
 81 sents the most established modality for pore typing studies (Skalinski & Kenter, 2015;
 82 McCreech et al., 1991).

83 Visual pore-typing involves user classification of observed pores into types accord-
 84 ing to popular schema, such as those proposed by Choquette and Pray (1970), Lucia (1983),
 85 Lucia (1995), and Lønøy (2006). Presently, visual pore-typing is conducted in a qual-
 86 itative to semi-quantitative fashion (i.e., via point-counting), a practice that has evolved
 87 little since its inception. Barring the inefficiency, subjectivity, and lack of scalability of
 88 manual approaches, integrating qualitative / semi-quantitative descriptions into reser-
 89 voir characterization schemes remains challenging, primarily due to the quantitative na-
 90 ture of the other input data modalities (e.g., well-logs, seismic lines, core plug petrophys-
 91 ical measurements, etc.) (Rabbani et al., 2021).

92 Recent studies have attempted to automate the process of visual pore-typing, fu-
 93 eled by recent advances in artificial intelligence (AI), and computer vision (CV). These
 94 studies attempt to emulate the heuristics employed by geologists when classifying pores
 95 by hypothesizing that all pores can be differentiated into their genetic classes purely based
 96 on shape. The de facto approach these studies employ is to use supervised machine learn-
 97 ing models within an object-based framework, where the segmented pores are represented
 98 as objects with size and shape metadata attached (Abedini et al., 2018; Borazjani et al.,
 99 2016; Ghiasi-Freez et al., 2012; Mollajan et al., 2016; Z. Wang et al., 2022), as summa-
 100 rized in Table S1 (in supplementary information). Object-based methods are arguably
 101 more intuitive for quantitative pore-typing from petrographic images when compared to
 102 texture-based methods, as it is easier to recognize geological discontinuities by their size
 103 and shape than by their pixel features. Object-based approaches have also become the
 104 gold standard in remote sensing studies, collectively referred to as Geographic Object-
 105 based Image Analysis (GEOBIA) (Blaschke, 2010).

106 Another shared feature amongst most automated pore-typing studies is the use of
 107 simple shape features. In the context of pore typing, shape is defined as the geometric
 108 features of an object after its location, orientation, and size are removed (Neal & Russ,
 109 2012). Shape features sensitive to location, orientation, and size should be treated with
 110 caution (Loncaric, 1998; Neal & Russ, 2012). A useful framework for shape features is
 111 the quadrant shown in Fig. 1a. Simple shape features consist of combining size features
 112 (such as area, perimeter, maximum axial length of best fit ellipse, etc.) such that the out-
 113 put is a dimensionless ratio (e.g., the ratio of the longest axis to the shortest axis: as-
 114 pect ratio), in order to remove the influence of scale. While having the benefit of being
 115 intuitive and easy to implement, simple shape features also carry the drawback of be-
 116 ing non-unique, as several different shapes may have similar feature values (Loncaric, 1998;
 117 Neal & Russ, 2012). Conversely, complex shape features, such as Fourier descriptors (har-
 118 monic analysis) and moments analyses, while difficult to explain and implement, can re-
 119 construct the original shape of an object and are therefore considered unique to each ob-
 120 ject (Neal & Russ, 2012). Another critical requirement for shape features is independence
 121 (Loncaric, 1998). Each feature must measure unique aspects of the object shape to be

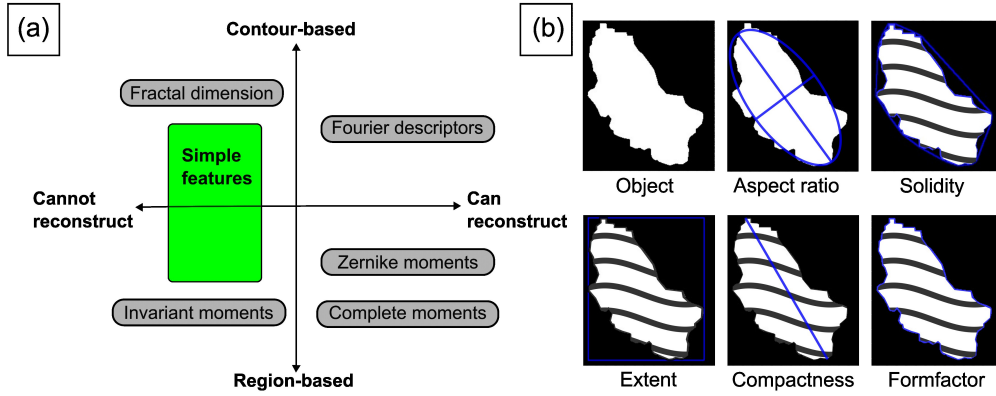


Figure 1. (a) Quadrant of shape features. Modified from (Neal & Russ, 2012). (b) Visual descriptions of the simple shape features used in this study.

122 informative. If multiple features measure the same property, redundancies occur. Sta-
 123 tistical analyses, particularly AI-based methods, can be severely hindered by such redun-
 124 dancies (James et al., 2021; Kuhn et al., 2013).

125 Relevant literature in the field of quantitative pore typing favor simple shape fea-
 126 tures to feed ML classifiers (Table S1), reporting testing accuracies well in excess of 90%.
 127 These results are remarkable given the complex pore types, such as interparticle, intra-
 128 particle, and microfractures (based on the Choquette and Pray (1970) scheme), classi-
 129 fied in these studies. Despite these promising results, none of the proposed solutions have
 130 widely proliferated within the wider petrographic community attached (Abedini et al.,
 131 2018; Borazjani et al., 2016; Ghiasi-Freez et al., 2012; Mollajan et al., 2016; Sharifi, 2022;
 132 Z. Wang et al., 2022), with most studies relying upon conventional manual interpreta-
 133 tion. This lack of uptake may, in part, be related to a general mistrust in the ostensi-
 134 bly optimistic results published, especially when considering that pore morphology is not
 135 the only determining factor when assigning pore types via conventional (i.e., qualitative)
 136 means.

137 Notably, there are deficiencies in four key areas within the literature: (1) the use
 138 of natively binary classifiers for multi-class problems, (2) the imbalanced and/or dimin-
 139 utive nature of the input datasets, (3) the lack of robust benchmarking, and (4) the mis-
 140 appropriation of deep learning. Classifiers that are natively binary (esp., Support Vec-
 141 tor Machines: SVM) have been employed to classify several different pore types (Mollajan
 142 et al., 2016; Sharifi, 2022). For context, binary classifiers can be extended to multi-class
 143 problems by condensing them into a series of binary classification problems, typically us-
 144 ing a one-versus-all (OVA) or one-versus-the-rest approach (Bishop, 2006; Galar et al.,
 145 2011; Mollajan et al., 2016). These approaches are conceptually problematic as the deci-
 146 sion boundaries from several binary classifiers are known to create ambiguous regions
 147 within the feature space, which can result in the same object being classified as differ-
 148 ent classes in different iterations (Bishop, 2006). Another inherent flaw is that models
 149 are trained on imbalanced data, as the class in focus will typically be diminutive com-
 150 pared to the other classes combined. Notably, such class imbalances are well-known to
 151 decrease model performance (Bishop, 2006; Galar et al., 2011; Chawla et al., 2004; He
 152 & Garcia, 2009; Sun et al., 2009). Furthermore, as the ‘other’ classes are typically merged
 153 for each classifier, any relationships or dependencies between classes may be ignored. In
 154 addition, since the number of binary classifiers will increase linearly with the number of

155 output classes, computational cost, and scalability can rapidly become limiting factors
156 (Bishop, 2006; Galar et al., 2011)

157 Supervised ML models are particularly sensitive to the nature of the labeled data.
158 Most related studies are opaque on their sampling protocols, which raises questions as
159 to whether the data was properly curated (Table S1) (e.g., Abedini et al., 2018; Boraz-
160 jani et al., 2016; Ghiasi-Freez et al., 2012; Mollajan et al., 2016; Sharifi, 2022; Z. Wang
161 et al., 2022). There are several indicators within the literature that point towards im-
162 proper dataset curation; firstly, the aforementioned studies contain severe class imbal-
163 ances in their training and testing data, which tends to give rise to model instabilities
164 and poor performance (Bishop, 2006; Galar et al., 2011; Chawla et al., 2004; He & Gar-
165 cia, 2009; Sun et al., 2009) / (Table S1). Secondly, their sample sizes are limited, even
166 going as low as five objects per class within some studies (Table S1) (Abedini et al., 2018;
167 Ghiasi-Freez et al., 2012; Mollajan et al., 2016). The sample sizes are far too insufficient
168 for the complexity pursued to produce robust models (Sun et al., 2009). Finally, several
169 pore types classified are not perceived by shape alone but by the spatial context of skele-
170 tal, depositional, and diagenetic components. For example, pore types such as vugs, molds,
171 intraparticle, interparticle, and intercrystalline pores cannot be differentiated by shape
172 but by examining their local neighborhoods. This raises questions about the subjectiv-
173 ity of the labelling process and, therefore, the validity of the training and testing dataset.

174 There is also a noticeable lack of model benchmarking within the related literature,
175 with supervised machine learning models being arbitrarily chosen to perform a given clas-
176 sification task (Table S1). In addition, several studies embrace deep learning (DL) mod-
177 els, despite the ‘excellent’ performance of ML models (Abedini et al., 2018; Borazjani
178 et al., 2016; Mollajan et al., 2016; Sharifi, 2022; Ansari, Abdalla, et al., 2022). The as-
179 sociated datasets do not meet the typical class balance and quantity requirements to en-
180 sure DL model generalizability. Also, these studies do not provide metrics such as validation-
181 loss curves to provide assurances on the model’s accuracy and stability.

182 A more equitable approach would be to condense pore-typing into a binary clas-
183 sification problem, such as distinguishing between microfractures and pores, as they rep-
184 resent visually distinct endmembers in morphology and are distinct in the mode of gen-
185 esis. This framing plays to the strength of most supervised ML classifiers as some were
186 designed to be binary classifiers (Multiple Logistic Regression and SVM, among others),
187 and single decision boundaries between two classes are far simpler to construct for any
188 model (Bishop, 2006; Galar et al., 2011; James et al., 2021; Kuhn et al., 2013; Kuhn &
189 Silge, 2022; Ansari, Yang, et al., 2022). In addition, binary classifications also enable ad-
190 ditional model performance metrics such as the Receiver Operating Characteristic (ROC)
191 curves (James et al., 2021; Kuhn et al., 2013; Kuhn & Silge, 2022). It is important to
192 note that while performance metrics such as ROC curves can be extended for multi-class
193 problems, it is far more challenging to implement and interpret. Once the end members
194 have been satisfactorily classified and decision boundaries established, it should be pos-
195 sible to analyze intra-class datasets to make finer distinctions between pore and microfrac-
196 ture types. Additionally, due to the ease of recognizing microfractures from pores, the
197 quality of the labeling data would be significantly higher than dividing the pores into
198 genetic types.

199 Only two studies have employed the binary approach within macrofractures in micro-
200 CT models (Li et al., 2017; Singh et al., 2021), and one in the case of microfractures (Z. Wang
201 et al., 2022). Li et al. (2017) utilized an SVM to separate macrofractures from vugs us-
202 ing simple shape features, reporting an accuracy of 100%. However, the authors did not
203 offer sufficient details on the modeling procedure, and from the images provided, the macrofrac-
204 tures appeared simplistic (short and straight). Singh et al. (2021) comprehensively demon-
205 strated segmentation of macrofractures and pores (with classification accuracies above
206 96%) using a projection-based clustering approach comprised of Principal Components
207 Analysis (PCA) and k-means clustering. However, the proposed method cannot be scaled

208 down to microfractures, given that size itself served as a major discriminator between
209 the macrofractures and pores. Z. Wang et al. (2022) reported near-perfect accuracies,
210 nullifying the challenge of classifying microfractures and pores. However, their classifi-
211 cation methodology was not described in detail, and the objects sampled for classifica-
212 tion were heavily curated and too few to be considered representative.

213 We propose that employing simple shape features for object classification within
214 a supervised machine-learning framework can accurately determine microfractures from
215 pores. In this work, we pose two questions: firstly, how accurately can supervised mod-
216 els classify microfractures and pores using only simple shape features? We posit that the
217 combination of simple shape features within a supervised ML framework should accu-
218 rately capture the shapes of microfracture and pores, given that these shapes represent
219 morphological endmembers. We eschewed unsupervised models for this study as super-
220 vised models are known to be substantially stronger. However, we did include two cluster-
221 ing algorithms (K-means and DBSCAN) on the global dataset as a reference against
222 the supervised models results (Fig. S4). Secondly, provided a sufficiently high accuracy
223 from the supervised classifiers, we pose the question: what are the most informative sim-
224 ple shape features for differentiating microfractures and pores? We hypothesize that as-
225 pect ratio is the most important shape feature as elongation is the primary and most in-
226 tuitive discriminator between the two classes.

227 The hypotheses in this study were tested on 18 petrographic plane-polarized light
228 scans of complete thin sections. The provenance of the microfractures is not considered
229 in this study as it is irrelevant to the tested hypotheses. We notify the reader, given the
230 small size of the dataset, that the results of this study are meant to be explanatory and
231 should not be considered as the most accurate models available. It is intended that the
232 results of this study will serve as a substrate for the development of highly accurate clas-
233 sifiers in future work. More importantly, the study was designed to address the method-
234 ological deficiencies of the related literature in terms of data handling and supervised
235 ML modeling as per the guidelines provided by Artrith et al. (2021) and Greener et al.
236 (2022).

237 Finally, we chose not to pursue DL in this study for the following reasons: firstly,
238 we have not fully realized the potential of ML within geo-images, and secondly, the black
239 box nature of DL means that we replace human subjectivity with machine subjectivity,
240 limiting the ability to draw translatable insights from any resulting classification. Finally,
241 in similitude to many geoscientific applications, difficulties in procuring sufficient train-
242 ing and test data make DL impracticable for the present study. To our knowledge, this
243 study represents the only openly available dataset solely dedicated to microfractures and
244 pores of carbonate thin sections within the geosciences.

245 **2 Methods**

246 **2.1 Dataset**

247 We selected eighteen images for this study, sourced from a repository of plane-polarized
248 light scans of carbonate thin sections at Texas A&M University, College Station. The
249 thin sections were scanned whole using the Nikon CoolScan 8000 film scanner at a res-
250 olution of 6.35 microns/pixel. The thin sections were sourced from a wide variety of out-
251 crops and subsurface cores. A key criterion for selection was the presence of sufficient
252 open-mode microfractures and pores. Healed microfractures (microveins) were ignored
253 as they require a different form of segmentation and are not within the scope of this study.
254 Eleven of the thin sections were half-stained with Alizarin red and seven thin sections
255 were unstained. The staining, however, did not affect the pore segmentation as all the
256 thin sections were impregnated with blue epoxy. The scans and processed images of the

257 thin sections used and associated metadata is provided in the dataset in the GitHub repos-
258 itory of the study.

259 **2.2 Image processing and segmentation**

260 *2.2.1 Pre-processing*

261 A schematic diagram for the entire image processing and machine learning pipeline
262 is provided in Fig. 2. For brevity, only the pertinent information is provided in the text,
263 with the finer details of each stage provided in the Supplementary Information. The edges
264 of all images were cropped prior to pre-processing to remove the blank slide edges. The
265 images were of sufficient quality that pre-processing only required minimal denoising and
266 sharpening. For denoising, the non-local means filter was applied using the ‘Non-local
267 means denoising’ plugin from the Biomedgroup library in Fiji (Darbon et al., 2008). The
268 non-local means filter was chosen for its excellent edge-preserving capabilities (Buades
269 et al., 2011). An unsharp mask filter was used to restore the sharpness after denoising,
270 using the in-built tool within Fiji, tuned according to each image. The images post-denoising
271 and post-sharpening are included as part of the dataset attached in the supplementary
272 information.

273 *2.2.2 Segmentation*

274 The segmentation of the blue-epoxy-filled pores from thin sections only required
275 thresholding in the HSB (Hue-Saturation-Brightness) color space. However, the low res-
276 olution of the available thin-section scans presented complications for the segmentation
277 of microfractures. Microfractures that appeared visually continuous tended to be frag-
278 mented into several smaller segments after thresholding in the HSB space despite exten-
279 sive tuning of the thresholding parameters (Fig. S1). To increase the microfracture con-
280 nectivity, an independent segmentation was performed in the CIELAB color space, which
281 is a device-independent 3D color space that accurately maps all perceivable colors, thus
282 enabling comparison. The CIELAB segmented image was combined with the original HSB
283 segmented image after post-processing both images. While there was a notable increase
284 in the connectivity of several microfractures (examples shown in Fig. S2), several mi-
285 crofractures were still heavily fragmented. Moreover, microporous matrix zones and mi-
286 croporous grains were segmented as macropores as a byproduct of the aggressive seg-
287 mentation strategy. The sheer number of microporous zones rendered masking imprac-
288 ticable. For this study, they were approximated as pores, which is reasonable given the
289 similarities in terms of shape for both pore types. Finally, any compromised image re-
290 gions (e.g., scratch marks or air bubbles) were masked manually.

291 *2.2.3 Post-processing*

292 The post-processing pipeline was conducted on both the HSB and LAB binary masks
293 in parallel (Fig. 2). Binary masks from both color spaces had smaller pores that were
294 poorly resolved, whereby the perimeter of these objects becomes pixelated and/or suf-
295 fers from partial area effects. As a consequence, the true shape of the pore is lost, and
296 any downstream analysis will be flawed. A workaround is to visually estimate the small-
297 est pore size that is adequately resolved and cull all objects below this threshold. Some
298 studies, particularly in the SEM and Liquid Metal Injection (LMI) domain, refer to the
299 smallest pore that is adequately resolved as the practical pore resolution (PPR) (Hemes
300 et al., 2015). In this study, we visually estimated that the smallest pore size that was
301 adequately resolved was 30 pixels in area (equivalent to pores of 190.5 microns). A mor-
302 phological closing operation using a 4-connect was applied using the Gray Scale Attribute
303 Filter tool in the MorphoLibJ plugin in Fiji (Legland et al., 2016), with the conserva-
304 tive 4-connectivity protocol used to prevent microfractures from being removed. It must
305 be noted that, given the relatively poor pixel resolution, the smallest pore size chosen

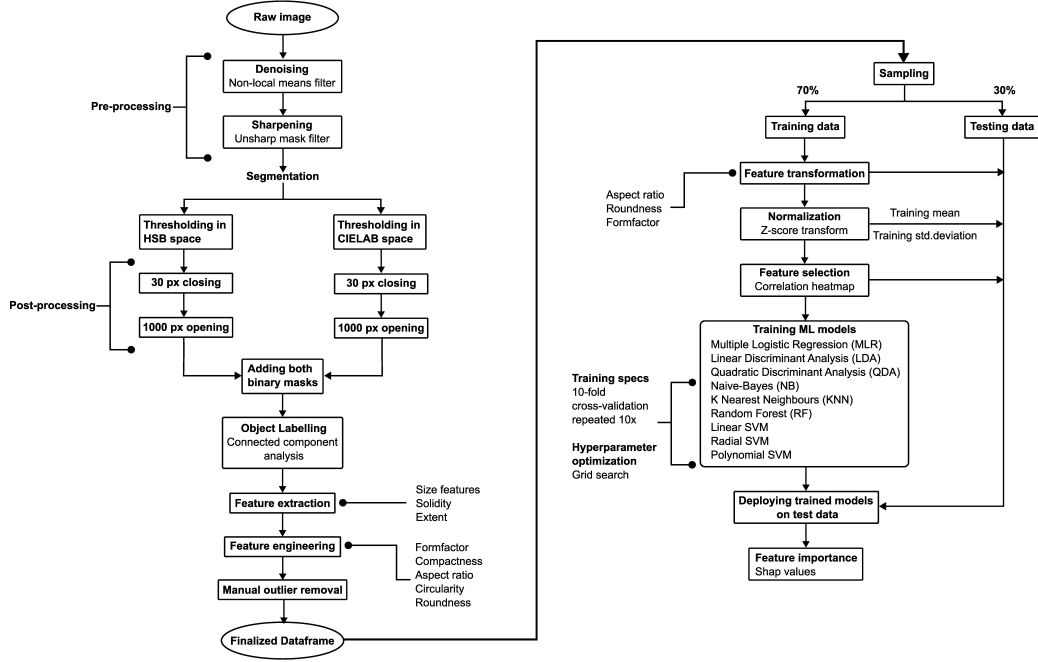


Figure 2. Flowchart of the digital image analysis and supervised modelling workflow.

306 is atypically aggressive, as even at this size, discretization effects are visible in several
 307 pores. This aggressive choice was warranted to preserve the microfractures since they
 308 were limited in quantity throughout the dataset. Additionally, several of the larger pores
 309 had floating objects within them (particles/air bubbles). These were removed from the
 310 objects via a morphological opening of 1000 pixels using the Gray Scale Attribute Fil-
 311 ter tool in the MorphoLibJ plugin in Fiji.

312 **2.3 Labelling, Feature Extraction and Feature Engineering**

313 The binary masks were imported into Python for labeling and feature extraction.
 314 The ‘Connected components’ function with 8-connect from the OpenCV library was used
 315 to label the microfractures and pores. The ‘regionprops’ module from the Sci-kit image
 316 library was used to extract the size and shape features of each object (Table 1). Shape
 317 features unavailable in the regionprop module but deemed necessary based on the lit-
 318 erature were calculated from the measured size metrics. We note here that eccentricity
 319 was discarded, despite its popularity as an elongation metric in the literature, as its dis-
 320 tribution was extremely right skewed even after Box-Cox transformations. Representa-
 321 tions of the selected shape features are shown in Fig. 1b.

Table 1: Feature Table

Feature	Equation	Definition	Shape aspect measured	Selected
Area	NA	The number of pixels of the object	None	No

Continued on next page

Table 1 – continued from previous page

Feature	Equation	Definition	Shape aspect measured	Selected
Filled area	NA	Number of pixels in the object with holes filled	None	No
Convex area	NA	Number of pixels in the convex hull of object	None	No
Perimeter	NA	The number of contour pixels	None	No
Crofton perimeter	NA	Perimeter of object approximated by Crofton formula in 4 directions	None	No
Major axis length	Normalized second central moments	The major axis of the best fitting ellipse	None	No
Minor axis length	Normalized second central moments	The minor axis of the best fitting ellipse	None	No
Equivalent diameter	NA	Diameter of the circle with equal area	None	No
Max feret diameter	NA	Maximum caliper length of object	None	No
Solidity	$\frac{\text{area}}{\text{area of convex hull}}$	Area of the object relative to its convex hull	Convexity	Yes
Extent	$\frac{\text{area}}{\text{area of bounding box}}$	Area of the object relative to its rigid bounding box	Complexity	Yes
Aspect Ratio	$\frac{\text{major axis length}}{\text{minor axis length}}$	Ratio of the major axis to minor axis	Elongation	Yes
Compactness	$\frac{\sqrt{4 \times \text{area} / \pi}}{\text{feret diameter max}}$	The ratio of the object area to its maximum Feret diameter	Elongation/circularity	Yes
Formfactor	$\frac{4 \times \pi \times \text{area}}{(\text{perimeter crofton})^2}$	Area- and contour-based circularity of the object	Circularity	Yes
Eccentricity	$\frac{\text{Distance from Focus}}{\text{Distance from Directrix}}$	Measure of the ellipticity of an object	Elongation/circularity	No
Circularity	$\frac{\text{equivalent diameter}}{\text{perimeter crofton}}$	Outline-based circularity of the object	Circularity	No
Roundness	$\frac{4 \times \text{area}}{\pi \times (\text{feret diameter max})^2}$	Area-based circularity of the object	Circularity	No

2.4 Statistical Analysis of the Extracted Features

2.4.1 Outlier Detection

Identifying outliers is a pre-requisite for building machine learning models, as they can hinder model performance and result in convergence to local minima. We omitted automated outlier detection methods (e.g., Tukey’s boxplot) due to the aggressive selection criteria such approaches employ. Aggressively removing a large chunk of true objects may improve model accuracy at the cost of generalizability, as the model will overfit to a heavily sanitized training dataset. Consequently, we employed a manual approach, whereby data points that were ten standard deviations from the mean of both size and shape features were visually corroborated with their corresponding thin-section image before being classified as outliers. This manual approach ensured that only the most prominent outliers per image were removed (2-5 per image), thus preserving the potential generalizability of the models. The total number of data points used for modeling was 20,060 after discarding outliers.

2.4.2 Sampling, Primary Labeling and Secondary Labeling

We applied different strategies to sample pores and microfractures, dictated by the limited number of microfractures in the images. Sampling for the pores was performed randomly, while microfractures were sampled manually. 400 microfractures and 400 pores were selected as the labeled dataset. The design of the sampling protocol was intended to maximize the quality of the ground truth. For 100 pores, sampling was performed with pore area greater than 100 pixels to ensure the larger pores were represented in the training and testing sets, given the strong skew towards smaller pores. Open gashes associated with microstylolites were avoided altogether, as these are discontinuities principally formed by pressure solution rather than brittle deformation. Moreover, open gashes were rarely observed in the dataset, and their omission is not expected to impact the results significantly.

To supplement the primary labels of ‘pore’ and ‘microfracture’, secondary labels were added to each sampled object pertaining to the type of pore or microfracture. Four types of microfracture were delineated by morphology based on the samples in this study: namely, straight, curvilinear, curved, and branching. These sub-categories were based on visual appearance and not on any established scheme. While labeling microfractures as straight and branching was relatively intuitive, the difference between curvilinear and curved was more subtle. Microfractures that were dominantly linear with negligible deviations were judged as curvilinear, whereas if there were major deviations in their trace morphology, they were classified as curved. Examples of these four types are shown in Fig. 3a. It should be noted that branching microfractures can be further subdivided into further shape-based categories (T-type / X-type, e.g., (Seers & Hodgetts, 2016)), though for parsimony, we avoided such higher-order classes in the present study. Conversely, pore types were defined by origin rather than morphology, namely vug, intercrystalline, intraparticle, and channel, as per the Choquette and Pray (1970). Vug was used as a catchall term applied to group relatively equant pores with evidence of genesis through dissolution and those with ambiguous origin. Intercrystalline pores were those housed within incompletely cemented spaces. Channels posed an interesting conundrum as they originated from microfractures but evolved into pores. However, apart from one sample, channels were rarely observed in the dataset and, therefore, poorly represented. We also point out that interparticle pores were rare in the dataset and, hence, were not represented during the random sampling. The inclusion of sufficient channels and interparticle pores in the training data should be a target for future work.

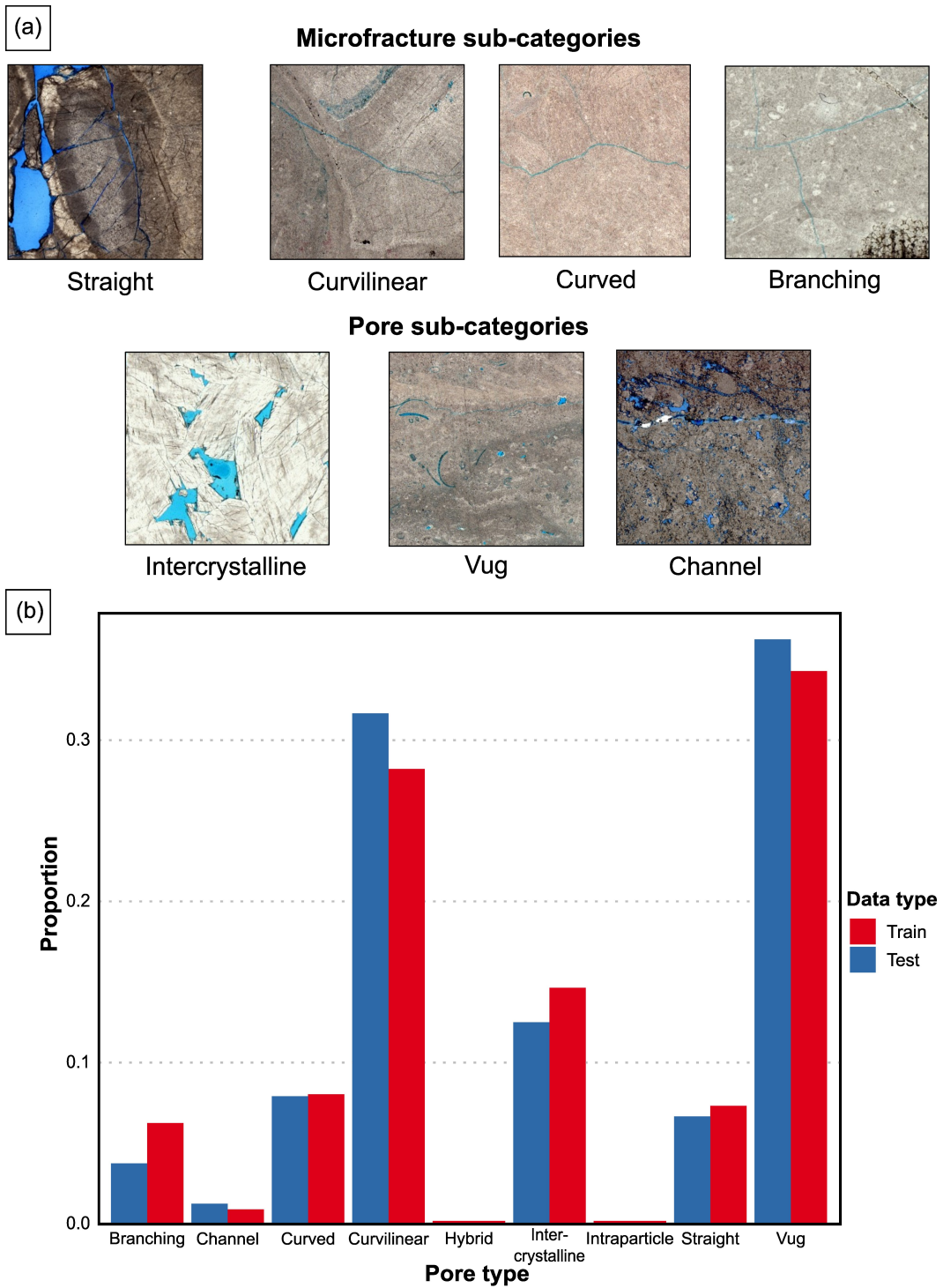


Figure 3. (a) Examples of pore and microfracture types from the dataset. (b) Proportion of pore and microfracture type in training data.

370 2.5 Supervised Machine Learning Pipeline

371 2.5.1 Training-Testing Split

372 The labeled dataset was split into 70% training and 30% testing subsets in a ran-
 373 domly stratified manner, keeping the proportions of pores and microfractures equal within
 374 both sets. This split resulted in 280 microfractures and pores in the training set and 120
 375 microfractures and pores in the testing set. The training-testing split was performed prior
 376 to the subsequent data processing to prevent data leakage.

377 2.5.2 Feature Transformation

378 All the shape features within the training data exhibited varying degrees of non-
 379 normality, with compactness and extent containing visible bimodality, and roundness,
 380 aspect ratio, and formfactor showing a degree of right skew. These right-skewed feature
 381 sets were log-transformed to balance their data range, mitigating data paucity and po-
 382 tentially increasing model accuracies. We emphasize that the transformation approach
 383 was not designed to satisfy the assumption of multivariate normality by parametric mod-
 384 els, such as multiple logistic regression (MLR), linear discriminant analysis (LDA), and
 385 quadratic discriminant analysis (QDA). The fact that several of the features, post-transformation,
 386 were significantly bimodal precludes the possibility of forcibly converting them into normal
 387 distributions. Moreover, Graf et al. (2022) showed that LDA is ostensibly robust against
 388 lognormal skewed and bimodal distributions, thus indicating that the assumption of nor-
 389 mality is not critical. Post-transformation, the features in the training and testing data
 390 were centered and scaled to ensure comparability between the features. We note that
 391 all features in the testing data were centered and scaled using the mean and standard
 392 deviation derived from the training data.

393 2.5.3 Feature Selection

394 Feature selection was entirely supervised based on a priori knowledge of the fea-
 395 tures and their correlations. As discussed above, feeding redundant features into ML mod-
 396 els can undermine each feature’s true impact and cause model instabilities: a problem
 397 known as multicollinearity (James et al., 2021; Kuhn et al., 2013). Furthermore, reduc-
 398 ing the number of features decreases the possibility of sparse distributions in feature space,
 399 often referred to as the ‘curse of dimensionality’ (Kuhn & Johnson, 2019). We expected
 400 high correlations between the features as each was derived from the same pool of size
 401 features. Features with Pearson’s correlation coefficient r^2 values exceeding 0.95 were
 402 candidates for elimination, a clause satisfied by roundness and circularity (Fig. 4). Round-
 403 ness was strongly correlated with compactness ($r^2 = 0.97$), which was expected as both
 404 features are essentially a ratio of the object area to its maximum Feret diameter. Due
 405 to their equivalence, compactness was preserved. Similarly, circularity and formfactor
 406 showed a similarly high correlation ($r^2 = 0.96$) as both features are a ratio of the ob-
 407 ject’s area to its perimeter, meaning either could be chosen (for this study, we chose form-
 408 factor). Aspect ratio was the only exceptional feature, as it was negatively correlated with
 409 every other feature, and in particular, compactness. The final features selected were form-
 410 factor, compactness, extent, solidity, and aspect ratio. The selected features are concep-
 411 tually independent of one another, with the exception of extent and solidity, which are
 412 both area-ratio variants, thus by-in-large, satisfying the independence requirement put
 413 forward by (Loncaric, 1998; Neal & Russ, 2012). A caveat to the feature selection pro-
 414 cess is that correlation analysis assumes univariate normality, an assumption that was
 415 violated by most of the features. However, since the correlation was only used to detect
 416 redundant features and was not involved in the modeling process, the impact of violat-
 417 ing the assumptions is not an issue.

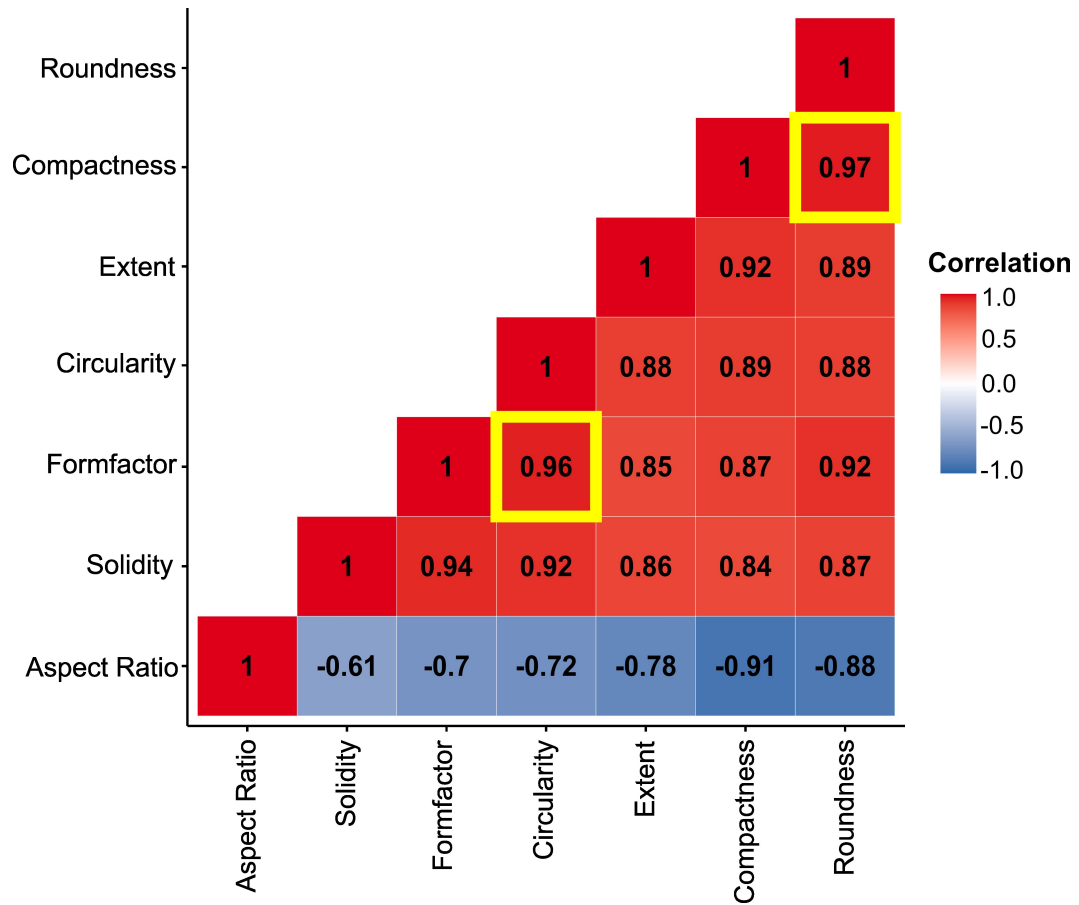


Figure 4. Correlation matrix of all input features. The yellow boxes mark the highest correlations among the features.

418 **2.5.4 High Dimensional Visualization: Principal Components Analy-** 419 **sis (PCA)**

420 Principal Components Analysis (PCA) was used to visualize the relationships in
 421 five-dimensional space. PCA is a wholly unsupervised technique that reduces the dimen-
 422 sionality of data to those that explain the maximal variance (Jolliffe & Cadima, 2016;
 423 Vogelstein et al., 2021). PCA is arguably the most popular dimensionality-reduction tech-
 424 nique (Vogelstein et al., 2021). Details on the conceptual and mathematical underpin-
 425 nings of PCA can be reviewed in Jolliffe and Cadima (2016). The covariance matrix of
 426 the dataset was constructed and factorized using eigen decomposition to find its prin-
 427 cipal components. We performed PCA on the whole dataset and the labeled subset, with
 428 the same processing steps used for the training and testing data applied to both datasets.

429 **2.5.5 Model Selection**

430 Several supervised ML models were tested as we had no prior knowledge as to which
 431 was best suited to our problem. This practice is colloquially known as the ‘No free lunch
 432 theorem’ (Kuhn & Silge, 2022). The ‘best’ model does not necessarily mean the most
 433 accurate, but rather the model that balances accuracy with generalizability and efficiency.
 434 We tested nine models in this study: multiple logistic regression (MLR), linear discrim-
 435 inant analysis (LDA), quadratic discriminant analysis (QDA), K-nearest neighbors (kNN),
 436 Naive-Bayes (NB), Random forest (RF), and three variants of Support Vector Machines
 437 (SVM); linear, radial, and polynomial. Further details on each model can be found in
 438 James et al. (2021) and Kuhn et al. (2013). These models can be broadly classified into
 439 two categories: linear and non-linear. Linear models generate linear decision boundaries
 440 in high-dimensional feature space, whereas non-linear models create non-linear decision
 441 boundaries in feature space such as polynomial, radial, or more complex non-parametric
 442 curves. All models were run using the ‘caret’ package in R (Kuhn, 2022).

443 **2.5.6 Hyperparameter Optimization**

444 Most of the tested models possessed hyperparameters that require user definition.
 445 Optimal parametrization is critical to maximize the performance of supervised models.
 446 For models without tunable hyperparameters, such as MLR, LDA, and QDA, the mod-
 447 els were trained using 10-fold cross-validation repeated ten times with accuracy as the
 448 chosen metric. For models that contained tunable hyperparameters, a grid search tech-
 449 nique was employed for each hyperparameter, with 10-fold cross-validation repeated ten
 450 times applied to each set of hyperparameters. The hyperparameter combination with the
 451 highest average accuracy was selected to train the final model. The list of the hyperpa-
 452 rameters for each model (if present) and the chosen values are provided in Table S2. The
 453 hyperparameter optimization curves for each of the models are provided in the supple-
 454 mentary information (Fig. S6) (hyperparameter optimization was implemented using the
 455 ‘trainControl’ function in the ‘caret’ library in R).

456 **2.5.7 Learning Curves**

457 Learning curves were generated for the models to assess their stability and to de-
 458 tect any overfitting (Fig. S6). Learning curves graphically represent how well the ML
 459 model learns the classification task on incrementally larger portions of a training dataset
 460 (Kuhn et al., 2013). The typical trend is a sharp increase in training accuracy at the start
 461 as the model learns new data, eventually leading to a plateau as the model masters the
 462 task. For this study, the training and resampling increments were set at 10% of the train-
 463 ing dataset. This meant 56 data points were used to train the model for the first run,
 464 with another 56 data points added for the second run. This incremental training was ex-
 465 ecuted for ten runs till the entire training dataset was used to train the model. To check
 466 for overfitting, at each of the ten learning stages, a randomly resampled subset of the

Table 2. Confusion Matrix

True positive Positive class predicted correctly as positive	False positive Negative class predicted incorrectly as positive
False negative Positive class predicted incorrectly as negative	True negative Negative class predicted correctly as negative

467 training dataset was used to test the accuracy of the model. The difference between the
 468 training and resampling curves is called the generalization gap. Typically, the lesser the
 469 gap, the more generalizable the model is considered to be (Kuhn et al., 2013).

470 **2.5.8 Model Accuracies**

471 As this is a binary classification study, the training and testing accuracy was mea-
 472 sured using a confusion matrix. A confusion matrix is composed of four options: true
 473 positive (TP), false positive (FP), true negative (TN), and false negative (FN), as de-
 474 fined in Table 2. Either of the classes can be designated as the positive class, with mi-
 475 crofractures denoted as positive. Correctly predicted microfractures were classed as TP,
 476 and correctly predicted pores were classed as TN, whereas incorrect predictions for each
 477 pore type fell under FP or FN. The training and testing accuracy was calculated using
 478 (1). Whilst accuracy gives an overall picture of how accurate the model is, it does not
 479 provide information about how well the model predicted each class separately. Sensitiv-
 480 ity, a measure of how accurately the model predicted the positive class (microfractures)
 481 (2), and specificity, a measure of how accurately the model predicted the negative class
 482 (pores), were calculated to address this deficiency (3).

$$\text{Accuracy} = \frac{\text{TP} + \text{TN}}{\text{TP} + \text{TN} + \text{FP} + \text{FN}} \quad (1)$$

$$\text{Sensitivity} = \frac{\text{TP}}{\text{TP} + \text{FN}} \quad (2)$$

$$\text{Specificity} = \frac{\text{TN}}{\text{TN} + \text{FP}} \quad (3)$$

483 **2.5.9 Feature Importance**

484 We used Shap values to evaluate the explanatory power of shape features. Initially
 485 intended to provide a means for the equitable distribution of winnings (Shapley, 1953;
 486 Lundberg & Lee, 2017), Shapley values have been appropriated from cooperative game
 487 theory into AI as a way to impute the importance of features in black-box models: a field
 488 now known as ‘Explainable AI’ (note that authors have coined the term ‘Shap values’
 489 to differentiate from the usage of Shapley values in Game Theory: (Lundberg & Lee, 2017)).
 490 Shap values are model-agnostic and post-hoc in that they are not part of the model-building
 491 process but instead offer an external check used to explain the feature contributions to
 492 predictions. It is important to note that Shap values calculate the local importance of
 493 features, which is the importance of a particular feature to specific data points. An ag-
 494 gregation is performed to provide the global importance of each feature with regard to
 495 the entire dataset. For this study, both the local and global importance were measured
 496 for each model. It is also essential to acknowledge that some of the models, as an inher-

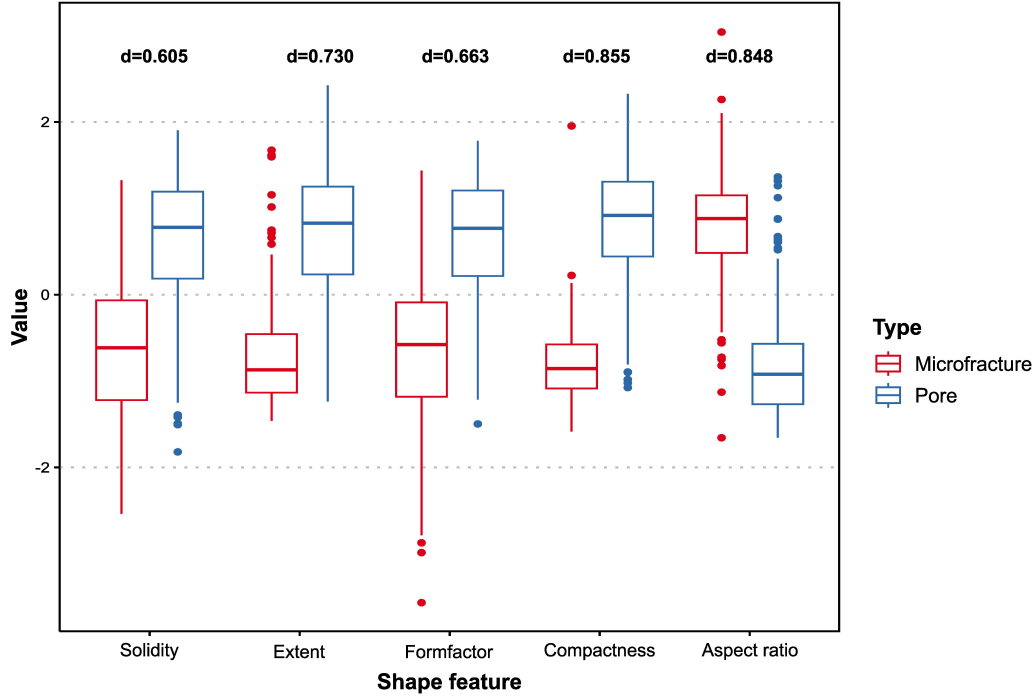


Figure 5. Differences in selected shape feature values between microfractures and pore, with the d-statistic reported for each feature. Each d-statistic was statistically significant to $p \ll 0.001$.

497 ent aspect of their mechanics, can list the features in order of importance, namely MLR,
 498 LDA, QDA, and RF. However, we computed Shap values for all models to ensure com-
 499 parison between the models.

500 3 Results

501 3.1 Statistical Analysis of the Extracted Features

502 3.1.1 Univariate Distributions

503 The shape features for the entire dataset displayed no bimodality (Fig. S3), thus
 504 precluding any trivial assignment of decision boundaries between microfractures and pores.
 505 The lack of clear bimodality suggests the need for a high-dimensional combinatorial ap-
 506 proach to separate the classes. However, in the labeled dataset, most of the shape fea-
 507 tures (aspect ratio, compactness, formfactor, and extent: Fig. S3) exhibited varying de-
 508 grees of bimodality related to the disparate signatures of microfractures and pores (Fig.
 509 5). However, the presence of intermediate values between the observed modes precludes
 510 the placement of straightforward decision boundaries. Visual inspection of the class pop-
 511 ulations of each shape feature suggests that compactness and aspect ratio exhibit the
 512 greatest separation between microfractures and pores, with solidity and formfactor show-
 513 ing the least difference, as quantified by the d-statistic from the Kolmogorov-Smirnov
 514 (K-S) test (Fig. 5).

515

3.1.2 PCA

516

517

518

519

520

521

522

523

524

525

526

527

528

The PCA biplot in the PC1-PC2 domain for the whole dataset (Fig. 6a) shows no discernable grouping but rather resembles a dense, compact cloud. The lack of separation is noteworthy, provided that PC1 and PC2 account for 93.76% of the variation in the data. The PCA visualizations containing the labeled data (Fig. 6b-c) show that the pores cluster in the direction of compactness, formfactor, and the area ratios (solidity and extent). Conversely, the more elongated microfractures cluster slightly away from the pores in the opposing direction of the aforementioned features, but in the direction of aspect ratio. It is also apparent that labeled microfractures offer a more tightly concentrated cluster, whereas the pores are more widely dispersed, with some pores overlapping within the microfractures cluster. There is also a noticeable separation between the loadings of the selected shape features, which supports the notion of independence previously alluded to. The separation of extent and solidity suggests that both features are potentially informative despite being similar area ratios.

529

530

531

532

533

534

535

536

537

538

539

540

541

The clustering of the labeled microfractures and pores becomes more evident when PCA is performed on the labeled dataset (Fig. 6c). PC1 and PC2 now explain a marginally higher proportion of the variance in the data (95.82%). Based upon the directions of the feature loadings, compactness and aspect ratio separate the two classes into two clusters. Furthermore, solidity and formfactor appear to extend both classes, but not sufficiently to form new clusters. This intra-class extension is further highlighted in Fig. 6d, where the datapoints are denoted by their secondary labels. In terms of pores, the two dominant pore types, intercrystalline, and vugs, show considerable overlap with no visible trend. Conversely, microfractures show a slightly discernible trend where the straight sub-class is concentrated at the base of the microfracture cluster (in the direction of increasing solidity and formfactor), and the branching and curved sub-classes concentrated near the top (in the direction of decreasing solidity and formfactor), with the curvilinear occupying the central portion of the variable space.

542

3.2 Supervised Machine Learning

543

544

545

546

547

548

549

Based on the learning curves (Fig. S6), all models show a narrow generalization gap, which indicates a lack of overfitting, except random forest, which showed overfitting to the training data (as the training accuracy was a constant 100%). In addition, most models appear to stabilize at roughly 300 data points, which points to the sufficiency of the training data for the models to learn the classification task. Another significant finding is that the linear models displayed stability and generalizability despite the lack of multi-variate normality within the training data.

Table 3. Training and testing accuracies for the supervised models

Model	Train Acc.	Train Kappa	Test Acc.	Test Kappa	95% Lower CI*	95% Upper CI*	Sens.	Spec.
MLR	94.48	88.96	90.00	80.00	85.49	93.49	96.67	83.33
LDA	94.00	88.00	89.58	79.17	85.01	93.14	97.50	81.67
QDA	94.29	88.57	90.83	81.67	86.45	94.17	97.50	84.17
kNN	94.70	89.39	90.00	80.00	85.49	93.49	94.17	85.83
NB	93.64	87.29	89.58	79.17	85.01	93.14	95.83	83.33
RF	94.11	88.21	90.00	80.00	85.49	93.49	96.67	83.33
LinearSVM	94.59	89.18	90.42	80.83	85.01	93.83	96.67	84.17
RadialSVM	94.55	89.11	90.00	80.00	85.49	93.49	96.67	83.33
PolySVM	94.63	89.25	90.00	80.00	85.49	93.49	95.83	84.17

*CI: Confidence Interval, Sens.: Sensitivity, Spec.: Specificity

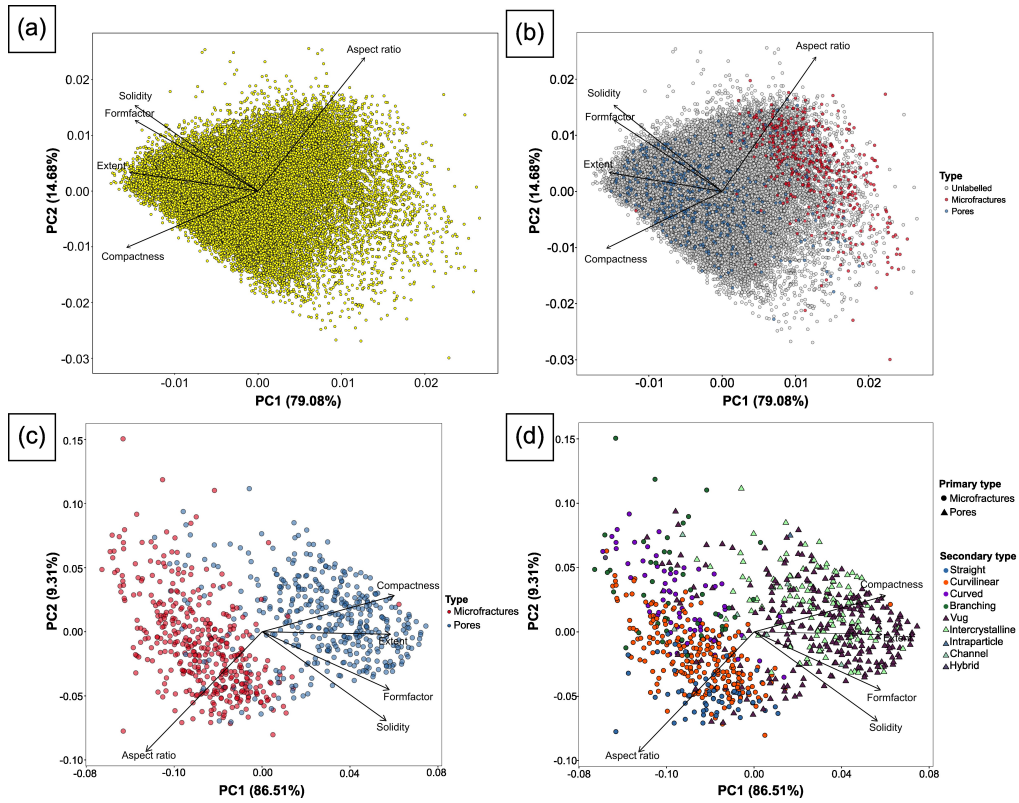


Figure 6. (a) Unlabelled PCA biplot with no separation between the datapoints. (b) PCA Biplot of the overall dataset with the labelled data overlaid. (c) PCA biplot of the labelled data. (d) Biplot of the labelled data with the secondary labels indicated.

550

3.2.1 Training Accuracy

551

552

553

554

555

All supervised models performed highly accurately, with a strikingly narrow envelope of 93.64% to 94.63% (Table 3). To facilitate comparison between the models, the upper and lower performance bounds were measured by resampling the same training data for each model. All models perform identically, with no apparent differences between the linear and non-linear supervised models.

556

3.2.2 Testing Accuracy

557

558

559

560

561

562

563

564

565

The excellent performances of the models on the training data were also reflected in the testing data. Testing accuracies were only slightly lower than those of the training set and had a similarly narrow performance envelope of 89.58% to 90.83%. All models appeared to detect microfractures with greater accuracy than pores, with testing sensitivities exceeding 95%, while specificities were capped at 86%. Furthermore, the ROC curves of all the models in Fig. 7a show Area Under Curve (AUC) values > 0.95 with no observable differences between them. Despite the conceptual differences between the models, similarities in performance strongly suggest that each model’s decision boundaries are similar and linear.

566

567

568

569

570

571

572

573

574

575

576

577

Despite the overall excellent performance of the models, there were systematic misclassifications. To better understand the misclassifications per model, the predicted microfracture probability of all the test data objects was derived for the sub-classes of microfractures and pores, as shown by the Polynomial SVM example in Fig. 8 (the plots for the other models are shown in Fig. S8). Most microfracture types are well above the 50% threshold across all models and, therefore, not likely to be predicted as pores. However, the branching sub-class shows the widest range of probabilities, dropping below 50% into pore prediction space in some cases. Amongst the pore types, vugs are the only class that spans nearly the entire probability range and are, therefore, responsible for the significantly lower specificities of the models. Upon closer examination, the vugs that cross the 50% threshold are dominantly bivalve molds (Fig. 8), which strongly resemble curvilinear microfractures.

578

3.2.3 Feature Importance

579

580

581

582

583

584

585

586

587

588

589

590

591

Shap plots ranking feature importance for all models are shown in Fig. S9 with only Polynomial SVM presented in Fig. 9 as a representative case. Feature rankings per model are listed in Table 4. Compactness was consistently the most important feature across models, while aspect ratio was the second-most important feature in most models tested (i.e., seven out of the nine), with MLR and LDA serving as the exceptions. Solidity was the third most important feature for most models, except for MLR and LDA (2), QDA (4), and Naive-Bayes (5). Solidity and formfactor appear to interchange positions in QDA and Naive-Bayes, which could be explained by their close correlation seen in the PCA biplot in Fig. 8b. The shape feature with the least contribution to most models is extent. It is also apparent that the models fall into three broad groups in terms of the feature importance profiles. The first group includes MLR and LDA, the second group includes the majority of the models, such as RF, KNN, linear SVM, radial SVM, and polynomial SVM, and the third group consists of QDA and Naive-Bayes.

592

4 Discussion

593

4.1 Performance of the Supervised ML models

594

595

596

The excellent performance of all the tested supervised ML models shows their efficacy in the presented classification task, in similitude to the high accuracies of supervised pore-type classification reported in the related literature (Table S1). However, a

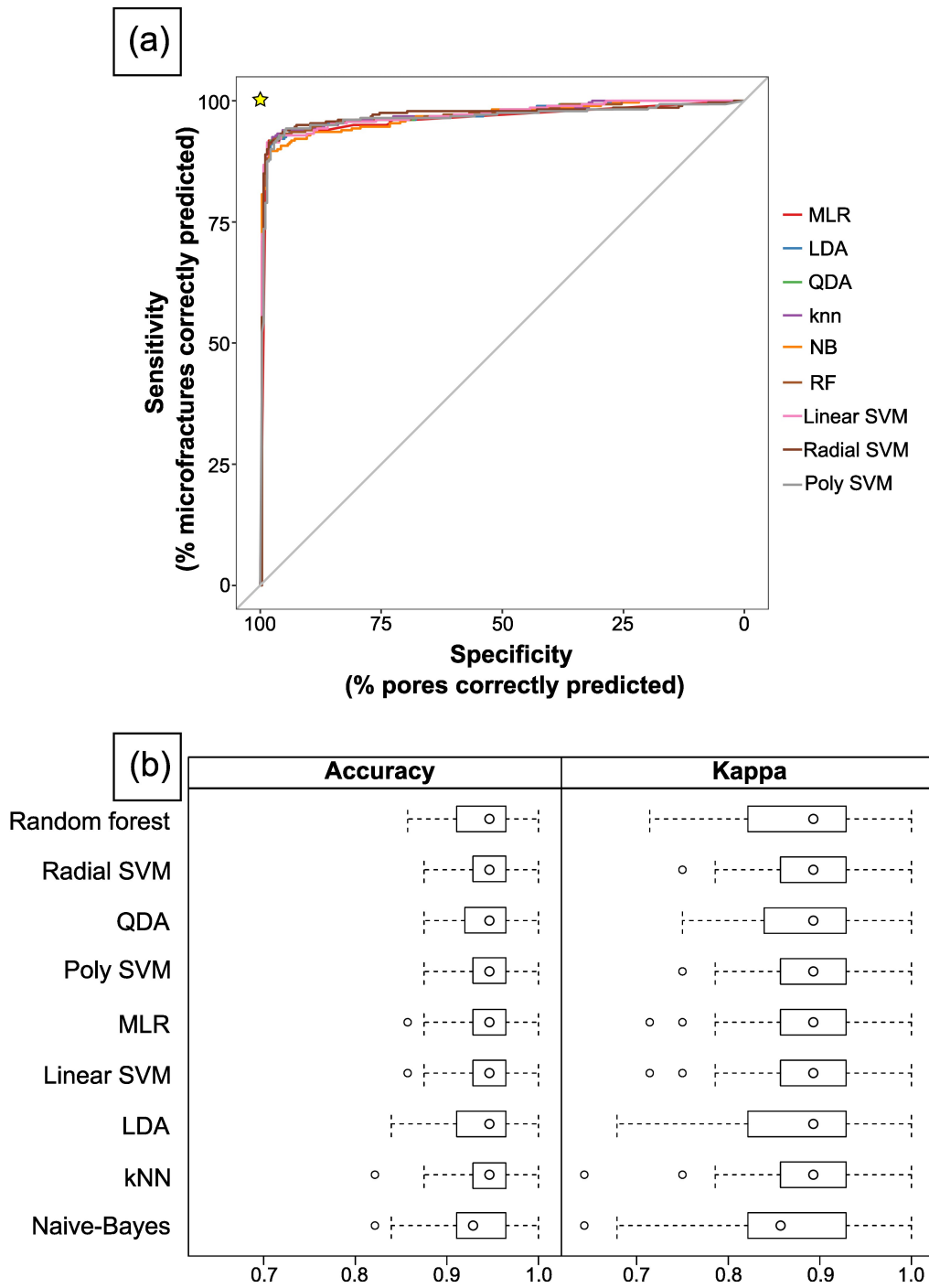


Figure 7. (a) ROC curves for all the tested models. All models show exceptionally high sensitivities and specificities across all probability thresholds. (b) Boxplot of training accuracies with confidence intervals derived from identical resampling.

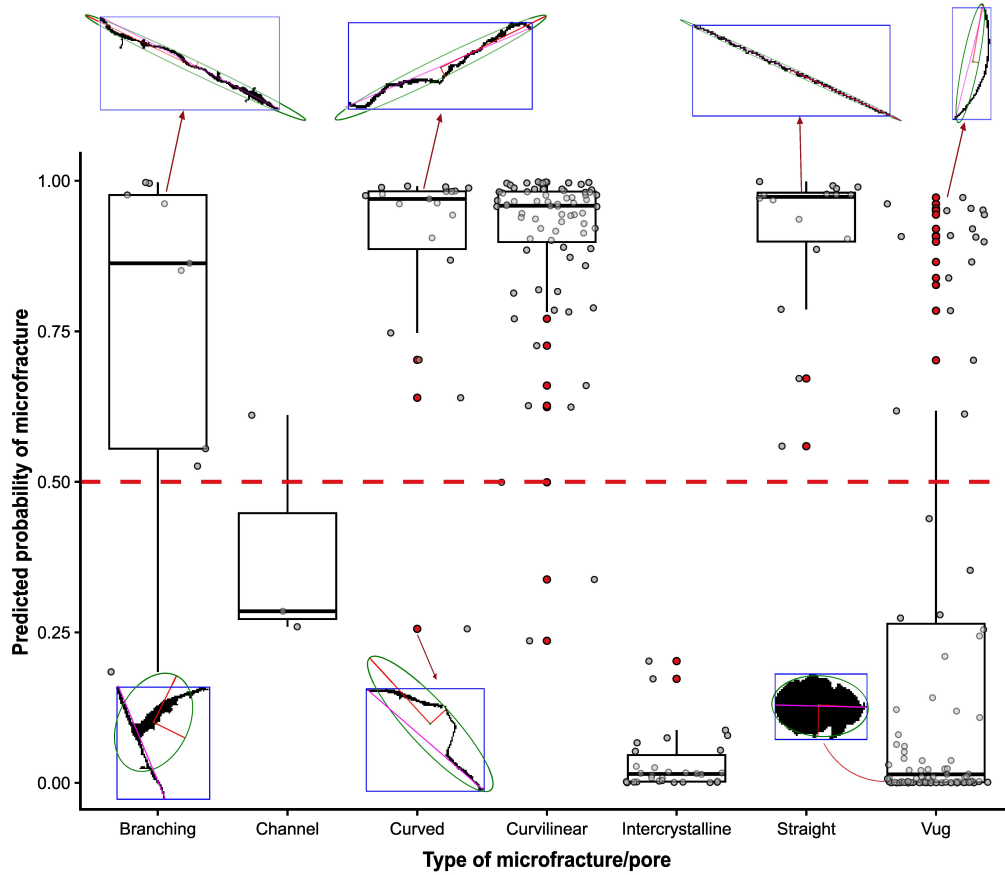


Figure 8. Microfracture prediction probability for each pore and microfracture type for Polynomial SVM model. Example masks of pore types are provided to illustrate the variation per class. The green ellipse represents the best-fitting ellipse with the red lines are the major and minor axes of the ellipse. The pink line represents the maximum Feret diameter. The blue box represents the bounding box.

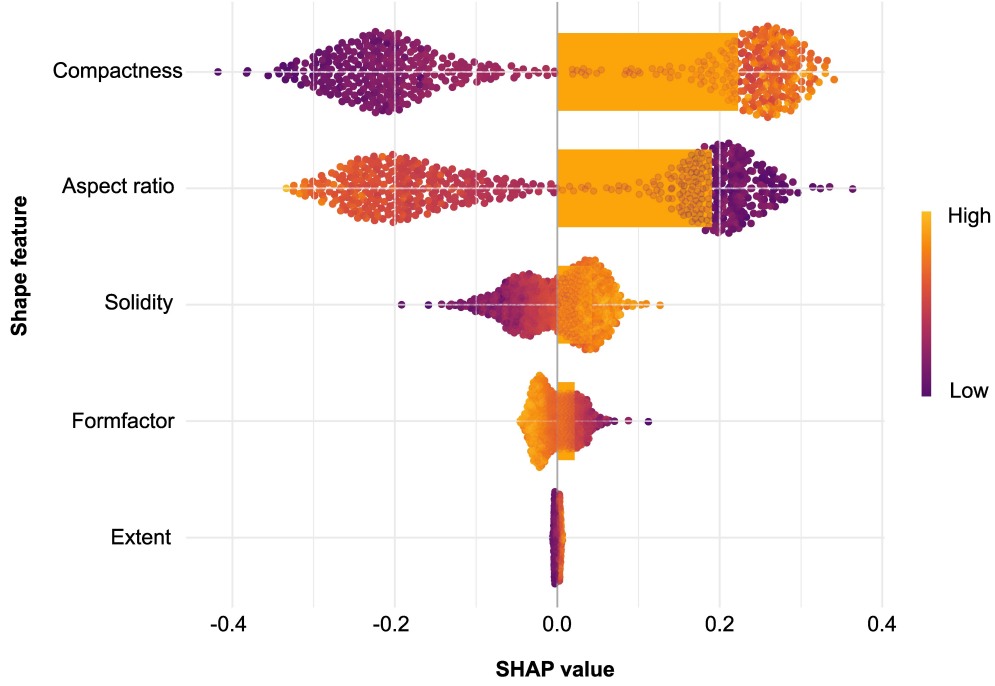


Figure 9. Shap values per feature for the Polynomial SVM model. The points represent local importance, and the bars represent global importance. The features are ordered by global importance.

Table 4. Rankings of the shape feature importance per model

	MLR	LDA	QDA	NB	kNN	RF	LSVM	RSVM	PSVM
Compactness	1	2	1	1	2	1	1	1	1
Aspect ratio	2	1	4	2	1	2	2	2	2
Solidity	5	3	2	5	3	3	3	3	3
Formfactor	3	4	3	4	4	4	4	4	4
Extent	4	5	5	3	5	5	5	5	5

597 straight comparison with the related literature is impossible due to the difference in the
 598 predicted classes. The equivalent performance of both linear and non-linear ML mod-
 599 els indicates ample separation between the microfractures and pores in the feature space,
 600 and the decision boundary was likely linear, thus posing a relatively simple classifica-
 601 tion task. Notably, this separation is discernable in the PCA biplot for the labeled data
 602 (Fig. 6c). Furthermore, all models contained errors related to the misclassification of bi-
 603 valves as microfractures, indicating that the models did not fit complex, non-linear de-
 604 cision boundaries through the microfractures cluster.

605 4.2 The importance of compactness and aspect ratio in the labelled dataset

606 The importance of compactness and aspect ratio in creating discernable separa-
 607 tion is evident from the PC1-PC2 visualization of the labeled data (Fig. 6c). Both fea-
 608 tures also ranked the highest amongst the shape features across most of the ML mod-
 609 els based on Shap values (Fig. 9 and Fig. S9). However, compactness consistently out-
 610 ranked aspect ratio across most models, which is perhaps counter-intuitive given the pop-

611 ularity of aspect ratio as a unique identifier for microfractures in the geological commu-
 612 nity (Table S1). To better understand the ranking, the aspect ratio of an object, using
 613 the best-fitting ellipse, essentially strips the object of its natural shape by assuming that
 614 two orthogonal axes can adequately represent it. We observe in Fig. 8 that best-fitting
 615 ellipses are reasonably faithful to the geometries of the more linear microfracture types
 616 (straight and curvilinear). In contrast, more curved or branched microfractures diverge
 617 from the low aspect ratio character and start to approach more pore-like values. Fig. 6d
 618 displays this to some extent, as the curving and branching microfractures are slightly
 619 closer to the pores than the straight variety. Conversely, compactness uses the original
 620 area of the object and only approximates its maximum length (the Feret diameter), which
 621 is a reasonably robust measure of object length and approximately equivalent to the ma-
 622 jor axis of the best-fitting ellipse. In addition, compactness places less weight on the area
 623 of the object and more emphasis on its maximum length: a construct that works well
 624 in the context of microfractures as they have significantly smaller areas than most sim-
 625 ilarly sized pores and always contain an outsized axis, except for a subset of branching
 626 microfractures. We note that any feature that adequately captures the salient charac-
 627 teristics of microfractures, namely the elongation and relatively narrow aperture, can con-
 628 tribute significantly to model performance. We also note that extent proved to be the
 629 least informative across all models. The lack of information can be attributed to its sen-
 630 sitivity to rotation, as illustrated in Fig. 8, where the same object can have different bound-
 631 ing boxes based on its orientation. Therefore, extent violates the rotation-invariance re-
 632 quirement of shape features (Loncaric, 1998). While extent contains information on the
 633 complexity of the pore (as more complex pores only take up a smaller portion of the bound-
 634 ing box), the rotation sensitivity means that solidity is a better replacement information-
 635 wise.

636 **4.3 The weaknesses of the approach when extended to the global dataset**

637 The results of the study indicate that the classification of microfractures and pores
 638 is a simple problem, which conforms to the visual perception that these pore types are
 639 separable by simple geometric features alone (Z. Wang et al., 2022). However, whether
 640 the labeled dataset of 800 points used in this study adequately represents the global dataset
 641 of 20,060 pores is questionable. Fig. 6a-6c highlights the major differences between both
 642 sets of data, with the unlabelled data showing none of the separation seen in the labeled
 643 data, thus strongly indicating that the classification is not straightforward. The differ-
 644 ence between the global and labeled datasets can be attributed to two main factors: ge-
 645 ological complexity and technical considerations.

646 **4.3.1 Complexity of Carbonate Pore Systems**

647 The complexity of carbonate pore types is well-known (Ehrenberg, 2022). Disso-
 648 lution and cementation are spatio-temporally variable processes controlled by a myriad
 649 of depositional and diagenetic agents, which typically result in complex pore morpholo-
 650 gies that often do not fit conveniently into classification schemes. The most popular of
 651 the pore-typing schemes, Choquette and Pray (1970), and Lucia (1983, 1995), do not con-
 652 tain morphology as a diagnostic attribute for this reason. To further highlight pore com-
 653 plexity, intercrystalline pores, and vugs overlap significantly in the PC1-PC2 space (Fig.
 654 6d) despite their contrasting origins attributable to cementation and dissolution, respec-
 655 tively. In addition, microfractures can develop complex morphologies (Fig. 8) based on
 656 the heterogeneity of the rock and the stress regimes acting therein.

657 **4.3.2 Non-unique Nature of Simple Shape Features**

658 Further to this, the non-unique nature of simple shape features used in this study
 659 and the related literature (Abedini et al., 2018; Borazjani et al., 2016; Ghiasi-Freez et

660 al., 2012; Mollajan et al., 2016; Z. Wang et al., 2022) could not adequately separate the
 661 pore types in hyperspace, as illustrated in Fig. 6a-d. These features can be informative
 662 for idealized objects where microfractures are mostly linear to curvilinear and pores are
 663 mostly equant. However, such scenarios are rare in the carbonate realm, and the con-
 664 tinued reliance upon simple feature sets will likely produce dense point clouds for which
 665 classification is problematic.

666 *4.3.3 Biased Sampling*

667 Selection bias during the sampling phase is a likely cause for the excellent separa-
 668 tion in the labeled data. In this study, operator discretion was required during the ran-
 669 dom sampling procedure to filter out noise, such as microporous patches or pores below
 670 the feature resolution. While this mitigated the noise fed into the models, it also meant
 671 that the most characteristic pores would be selected, thereby compromising the objec-
 672 tivity of the sampling procedure. Data curation is a typical stage for pore typing stud-
 673 ies, often resulting in overly optimistic results in supervised ML (Table S1). Compar-
 674 atively, most other related studies use at most 250 data points for labeling, while we used
 675 800.

676 It is evident that studies claiming excellent performance of supervised ML for pore
 677 typing have not fully considered the true complexity of the task and instead report the
 678 results of highly curated datasets (Abedini et al., 2018; Borazjani et al., 2016; Ghiasi-
 679 Freez et al., 2012; Mollajan et al., 2016; Z. Wang et al., 2022). We expect that this re-
 680 search avenue will continue to grow exponentially given the importance of automated
 681 pore-typing for a multitude of value-generating processes, mainly as we are well into the
 682 era of big data. Besides data curation, most related studies have only used a fraction of
 683 our ground truth size to build their models, which cannot be considered representative
 684 and will only exacerbate model accuracies (Abedini et al., 2018; Borazjani et al., 2016;
 685 Ghiasi-Freez et al., 2012; Mollajan et al., 2016; Z. Wang et al., 2022).

686 *4.3.4 Possible weaknesses within the projection method*

687 Another potential explanation for the lack of separation within the unlabelled data
 688 is the problematic nature of PCA with respect to the visualization of the feature space.
 689 While PCA is the most popular dimensionality-reduction approach within the scientific
 690 literature, it is also the weakest in projecting the true distances between points in 2D
 691 (Van Der Maaten et al., 2009; Thrun, 2018). In essence, large distances between points
 692 in feature space may appear close in the 2D-projected PCA space as PCA only rotates
 693 the data points to the axis containing the greatest variance. Unlike non-linear projec-
 694 tion methods, such as Connected Components Analysis (CCA), t-distributed Stochastic
 695 Neighbor Embedding (t-SNE), and Multi-dimensional Scaling (MDS), PCA does not
 696 disaggregate the data into clusters (Van Der Maaten et al., 2009; Thrun, 2018; Thrun
 697 & Ultsch, 2021). Therefore, PCA would unlikely display clusters unless the feature space
 698 already contains appreciable clustering within the higher dimensions. Hence, it can be
 699 argued that the unlabelled feature space may contain clusters by pore type that are col-
 700 lapsed into one another within the PCA space. It should be noted, however, that the density-
 701 based DBSCAN method only showed one cluster for the unlabelled data (Fig. S4b), and
 702 k-means only managed to bisect the cloud through its centroid (Fig. S4a). Both results
 703 are independent of the projection and suggest that there is no discernible separation be-
 704 tween the classes in the global feature space, which makes the use of any projection method
 705 moot for this case.

706 *4.3.5 Dataset Size*

707 Another factor that may have contributed to disparities in separability between the
 708 labeled and unlabeled data is the limited size of the dataset (18 images / 20060 objects),

709 which cannot be considered representative of carbonates. Several pore types commonly
 710 observed in carbonate studies, such as interparticle pores, intraparticle molds, and chan-
 711 nels, were limited in quantity, meaning that random sampling emphasized the more dom-
 712 inant intercrystalline pores and vugs. Including the former pores would potentially have
 713 resulted in a more complex feature space in the labeled dataset and be more represen-
 714 tative of the range of pore types observed within carbonate rocks. Indeed, even the ob-
 715 served spectrum of pore types within the 18 thin sections studied herein was not fully
 716 representative, as only 2% of the available pores were selected as ground truth compared
 717 to approximately 90% in the case of microfractures, thereby making this study more rep-
 718 resentative of the latter. Barring a community-wide effort, scant ground truth datasets
 719 for pore typing will likely continue to be a significant bottleneck for quantitative pore
 720 typing studies in carbonate lithologies.

721 **4.3.6 Fragmentation of microfractures**

722 Another likely cause for the separation in the labeled data was the microfractures’
 723 fragmentation due to the scans’ poor resolution. Several curved and branching microfrac-
 724 tures were fragmented into smaller, more linear segments, resulting in a disproportion-
 725 ate number of linear and curvilinear microfractures (Fig. S1). This over-simplification
 726 of complex microfracture networks masked the true complexity of the feature space. The
 727 geometric complexity of microfractures would be honored more accurately with higher-
 728 resolution scans, allowing the power of supervised ML models to be benchmarked more
 729 effectively. Spatial aliasing of fractures from image datasets is a ubiquitous issue related
 730 to their characterization (Seers & Hodgetts, 2014; Biber et al., 2018). We expect that
 731 the related literature also faced similar challenges related to resolution-dependent cen-
 732 soring of fracture networks reported herein, though it did not address it explicitly.

733 **4.4 Study Design Issues in Related Studies**

734 However, the larger problem with the related studies is that they bypass the sep-
 735 aration of microfractures and pores and directly classify pores into their sub-classes (Ta-
 736 ble S1). We show that there is heavy overlap between the pore types within the simple
 737 shape feature space, thus raising questions on the predictive accuracies of the proposed
 738 models in the literature. Again, the current dataset does not contain several pore types
 739 that share morphological similarities with microfractures, such as interparticle pores and
 740 channels, which would further convolute the feature space utilized for pore classification
 741 herein.

742 A related problem with most studies is that they do not explain the importance
 743 of the simple shape features in the ML models. The fact that all related studies re-use
 744 the same features without any explanation of their importance to the models only prop-
 745 agates poor practices in the field. For example, extent is commonly utilized within au-
 746 tomated pore typing studies (Table S1). However, we report that extent was the least
 747 informative feature across all models (i.e., based on the Shap values: Fig 9 and S9), due
 748 to its sensitivity to rotation violating the rotation-invariance requirement of shape fea-
 749 tures (Loncaric, 1998). While extent contains information on the complexity of the pore,
 750 as more complex pores take up a smaller portion of the bounding box, the rotation sen-
 751 sitivity means that solidity offers a more attractive alternative.

752 Finally, most related studies lack robust supervised ML methodologies (Abedini
 753 et al., 2018; Borazjani et al., 2016; Ghiasi-Freez et al., 2012; Mollajan et al., 2016; Shar-
 754 ifi, 2022; Z. Wang et al., 2022). Feature selection appears to be related more to the ease
 755 of acquisition rather than any proven utility. Most studies do not undertake visualiza-
 756 tion of the data in hyperspace using PCA (Abedini et al., 2018; Borazjani et al., 2016;
 757 Ghiasi-Freez et al., 2012; Mollajan et al., 2016; Z. Wang et al., 2022), thereby obfuscat-
 758 ing the underpinning drivers of their reported excellent model accuracies. Almost all re-

lated studies do not furnish details on hyperparameter tuning, perhaps as the default parameters produce excellent results (Abedini et al., 2018; Borazjani et al., 2016; Ghiasi-Freez et al., 2012; Mollajan et al., 2016; Z. Wang et al., 2022). Also, there needs to be more comparison across several different models, particularly with simpler classifier paradigms, to provide a baseline performance (Table S1).

4.5 Moving Forward

The classification of microfractures and pores is still a complex problem that requires attention. Given that these features are ostensibly geometric end members, it is more prudent to approach this problem prior to drawing finer distinctions in pore types using multiclass ML frameworks. Macrofracture segmentation studies follow this template with emphasis on extracting the macrofractures in microCT models by all possible means, with the other class inherently being pores (Lee et al., 2021). Ideally, enhancing the separation of microfractures and pores into natural clusters in the feature space should be prioritized. The presence of natural clusters would enable the use of unsupervised clustering models directly on the dataset or even on the dimensionally reduced projection (referred to as projection-based clustering) (Van Der Maaten et al., 2009; Thrun, 2018; Singh et al., 2021; Thrun & Ultsch, 2021). An unsupervised approach is scalable and has the added benefit of not requiring labeled data. However, natural clustering in the feature space is not likely using simple shape features. We hypothesize that more complex shape features such as the contour-based Fourier descriptors and region-based invariant moments (invariant Hu moments and Zernike moments) might create better separations in hyperspace, albeit with an attendant decrease in explainability of the features (Neal & Russ, 2012; Singh et al., 2021). It is also possible that in concert with more complex features, more powerful methods of dimensionality-reduction, such as CCA, MDS, and t-SNE, may enhance the presence of natural clusters for projection-based clustering (Thrun, 2018; Thrun & Ultsch, 2021). We note that a DL approach would likely offer the best results; however, to be feasible, it would require data sharing and ground truth labeling on a hitherto unprecedented scale within the geoscience community. It is pertinent to not only have a global representation of pore and microfracture types but also of a range of instruments with different acquisition parameters to ensure the generalizability of the classifiers. It would also require a community effort to find the best shape features and AI models, potentially borrowing from equivalent studies within the fields of computer vision and bioinformatics, for example, where similar applications of supervised and unsupervised machine learning towards object clustering and classification from image data is already mature (Butler et al., 2018; Chen et al., 2019; Doerr & Florence, 2020; Stafford et al., 2020; Urbanowicz et al., 2020; A. Y.-T. Wang et al., 2020). Studies utilizing limited data, such as the present study, are likely to succumb to the problems of lack of representation, selection bias, and technical issues related to the imaging process, which can be conveniently masked by overly optimistic results that cannot be translated to other datasets (Sun et al., 2009).

The findings of this study serve as a benchmark for ideal datasets with limited scope of pore types. Even simple linear models such as MLR and LDA can perform excellently within such scenarios. However, we argue that the overly optimistic results from related supervised ML studies using only simple shape features are more reflective of the sampling process than the underlying geometric complexity of the pore system. We also emphasize the methodological requirement of measuring the feature importance based on the PCA loadings and their Shap values per model. This essential exploratory data analysis step will ensure that only the most important features will be carried forward into future studies rather than needlessly recycled.

5 Conclusions

All the tested supervised models performed excellently in discriminating between microfractures and pores, with testing accuracies approaching 90% for all models. Notably, all tested supervised models exhibited near identical performance, indicating a significant separation between the two classes in hyperspace such that a linear boundary was adequate. The presence of a linear decision boundary was further supported by PCA visualization of the hyperspace and the systematic misclassification of bivalve molds as microfractures. However, upon comparing the feature spaces of the labeled data and the overall dataset, it is apparent that the labeled feature space presented a highly sanitized version of the larger dataset despite efforts toward the development of an objective sampling scheme. The sanitized dataset converted a complex problem requiring complex non-linear decision boundaries to a simple, linearly separable problem. While our study can provide a useful benchmark for those that contain more idealized datasets with limited microfracture and pore types, we demonstrate that the pore-typing problem is more complex than postulated by the related literature. Finally, we report that, contrary to expectations, compactness contributed more towards the ML classification of microfractures from pores than aspect ratio, as compactness only approximates one measure of the object compared to the two metrics approximated by aspect ratio. These results serve as a useful template for future studies on this first-order challenge of separating microfractures and pores and on higher-order challenges involving more complex multiclass pore typing.

6 Open Research

The image data used for the classification in the study and the R code developed are published at the GitHub repository for this study via <https://github.com/issacsujay92/Microfractures-And-Pores-ML> with no restriction on usage. The entire code was developed in R (version 4.2.1) (R Core Team, 2022) using the RStudio IDE. Figures were made using ggplot2 package (Wickham, 2016). The ML models were run using 'caret' version 6.0.93 (Kuhn, 2022). Data analytics and visualizations were implemented using the following packages: 'tidyverse' (Wickham et al., 2019), 'MASS' (Venables & Ripley, 2002), 'factoextra' (Kassambara & Mundt, 2020), 'FactoMineR' (Lê et al., 2008), 'ggfortify' (Tang et al., 2016), 'GGally' (Schloerke et al., 2021), 'klaR' (Weihs et al., 2005), and 'reshape2' (Wickham, 2007). Model performance evaluation was implemented using the 'MLeval' package (John, 2020). fastshap (Greenwell, 2021), and shapviz (Mayer, 2023) were essential to implementing and visualizing the Shap values for the ML models. The dataset used for this study is published in Harvard Dataverse (Jayachandran, 2023). The dataset is free to use without any restrictions.

Acknowledgments

The authors thank Dr. Siddarth Misra and Dr. Jim Ji for guiding the project from the inception. Dr. David Bapst and Dr. Christina Belanger are thanked for discussions during early versions of the draft and for their excellent course on implementing R for geological datasets. Issac would also like to thank Dr. Ankita Singh for enlightening discussions on the technical aspects of the study and the bigger picture implications. The authors are also grateful to Dr. John Russ for his permission to re-use a figure from his work. The financial assistance of Qatar Foundation, the Qatar National Research Fund (NPRP12S-0302-190194), and Total Energies Qatar are gratefully acknowledged by the authors.

References

Abedini, M., Ziaii, M., Negahdarzadeh, Y., & Ghiasi-Freez, J. (2018). Porosity

- 856 classification from thin sections using image analysis and neural networks in-
 857 cluding shallow and deep learning in jahrum formation. *Journal of Mining and*
 858 *Environment*, 9(2), 513–525.
- 859 Ansari, M. Y., Abdalla, A., Ansari, M. Y., Ansari, M. I., Malluhi, B., Mohanty, S.,
 860 ... others (2022). Practical utility of liver segmentation methods in clinical
 861 surgeries and interventions. *BMC medical imaging*, 22(1), 1–17.
- 862 Ansari, M. Y., Yang, Y., Balakrishnan, S., Abinahed, J., Al-Ansari, A., Warfa, M.,
 863 ... others (2022). A lightweight neural network with multiscale feature en-
 864 hancement for liver ct segmentation. *Scientific reports*, 12(1), 14153.
- 865 Anselmetti, F. S., Luthi, S., & Eberli, G. P. (1998). Quantitative characterization
 866 of carbonate pore systems by digital image analysis. *AAPG bulletin*, 82(10),
 867 1815–1836.
- 868 Artrith, N., Butler, K. T., Coudert, F.-X., Han, S., Isayev, O., Jain, A., & Walsh, A.
 869 (2021). Best practices in machine learning for chemistry. *Nature chemistry*,
 870 13(6), 505–508.
- 871 Biber, K., Khan, S. D., Seers, T. D., Sarmiento, S., & Lakshmikantha, M. (2018).
 872 Quantitative characterization of a naturally fractured reservoir analog using a
 873 hybrid lidar-gigapixel imaging approach. *Geosphere*, 14(2), 710–730.
- 874 Bishop, C. M. (2006). *Pattern recognition and machine learning* (Vol. 4) (No. 4).
 875 Springer.
- 876 Blaschke, T. (2010). Object based image analysis for remote sensing. *ISPRS journal*
 877 *of photogrammetry and remote sensing*, 65(1), 2–16.
- 878 Borazjani, O., Ghiasi-Freez, J., & Hatampour, A. (2016). Two intelligent pat-
 879 tern recognition models for automatic identification of textural and pore
 880 space characteristics of the carbonate reservoir rocks using thin section im-
 881 ages. *Journal of Natural Gas Science and Engineering*, 35, 944-955. Re-
 882 trieved from [https://www.sciencedirect.com/science/article/pii/](https://www.sciencedirect.com/science/article/pii/S1875510016306886)
 883 [S1875510016306886](https://www.sciencedirect.com/science/article/pii/S1875510016306886) doi: <https://doi.org/10.1016/j.jngse.2016.09.048>
- 884 Breiman, L. (2001). Random forests. *Machine learning*, 45, 5–32.
- 885 Buades, A., Coll, B., & Morel, J.-M. (2011, September). Non-local means denoising.
 886 *Image Processing On Line*, 1, 208–212. Retrieved from [https://doi.org/10](https://doi.org/10.5201/ipo1.2011.bcm_nlm)
 887 [.5201/ipo1.2011.bcm_nlm](https://doi.org/10.5201/ipo1.2011.bcm_nlm) doi: 10.5201/ipo1.2011.bcm_nlm
- 888 Butler, K. T., Davies, D. W., Cartwright, H., Isayev, O., & Walsh, A. (2018).
 889 Machine learning for molecular and materials science. *Nature*, 559(7715),
 890 547–555.
- 891 Chawla, N. V., Japkowicz, N., & Kotcz, A. (2004, jun). Editorial: Special is-
 892 sue on learning from imbalanced data sets. *SIGKDD Explor. Newsl.*, 6(1),
 893 1–6. Retrieved from <https://doi.org/10.1145/1007730.1007733> doi:
 894 [10.1145/1007730.1007733](https://doi.org/10.1145/1007730.1007733)
- 895 Chen, P.-H. C., Liu, Y., & Peng, L. (2019). How to develop machine learning models
 896 for healthcare. *Nature materials*, 18(5), 410–414.
- 897 Choquette, P. W., & Pray, L. C. (1970, 02). Geologic Nomenclature and Clas-
 898 sification of Porosity in Sedimentary Carbonates1. *AAPG Bulletin*, 54(2),
 899 207-250. Retrieved from [https://doi.org/10.1306/5D25C98B-16C1-11D7-](https://doi.org/10.1306/5D25C98B-16C1-11D7-8645000102C1865D)
 900 [-8645000102C1865D](https://doi.org/10.1306/5D25C98B-16C1-11D7-8645000102C1865D) doi: 10.1306/5D25C98B-16C1-11D7-8645000102C1865D
- 901 Cortes, C., & Vapnik, V. (1995). Support-vector networks. *Machine learning*, 20,
 902 273–297.
- 903 Darbon, J., Cunha, A., Chan, T. F., Osher, S., & Jensen, G. J. (2008, May). Fast
 904 nonlocal filtering applied to electron cryomicroscopy. In *2008 5th IEEE inter-*
 905 *national symposium on biomedical imaging: From nano to macro*. IEEE. Re-
 906 trieved from <https://doi.org/10.1109/isbi.2008.4541250> doi: 10.1109/
 907 [isbi.2008.4541250](https://doi.org/10.1109/isbi.2008.4541250)
- 908 Doerr, F. J., & Florence, A. J. (2020). A micro-xrt image analysis and machine
 909 learning methodology for the characterisation of multi-particulate capsule
 910 formulations. *International journal of pharmaceuticals: X*, 2, 100041.

- 911 Ehrenberg, S. (2022). The etiology of carbonate porosity. *AAPG Bulletin*, *106*(12),
912 2351–2386.
- 913 Ester, M., Kriegel, H.-P., Sander, J., Xu, X., et al. (1996). A density-based algo-
914 rithm for discovering clusters in large spatial databases with noise. In *kdd*
915 (Vol. 96, pp. 226–231).
- 916 Galar, M., Fernández, A., Barrenechea, E., Bustince, H., & Herrera, F. (2011). An
917 overview of ensemble methods for binary classifiers in multi-class problems:
918 Experimental study on one-vs-one and one-vs-all schemes. *Pattern Recogni-
919 tion*, *44*(8), 1761-1776. Retrieved from [https://www.sciencedirect.com/
920 science/article/pii/S0031320311000458](https://www.sciencedirect.com/science/article/pii/S0031320311000458) doi: [https://doi.org/10.1016/
921 j.patcog.2011.01.017](https://doi.org/10.1016/j.patcog.2011.01.017)
- 922 Ghiasi-Freez, J., Soleimanpour, I., Kadkhodaie-Ilkhchi, A., Ziaii, M., Sedighi, M.,
923 & Hatampour, A. (2012). Semi-automated porosity identification from thin
924 section images using image analysis and intelligent discriminant classifiers.
925 *Computers & geosciences*, *45*, 36–45.
- 926 Graf, R., Zeldovich, M., & Friedrich, S. (2022). Comparing linear discriminant
927 analysis and supervised learning algorithms for binary classification—a method
928 comparison study. *Biometrical Journal*.
- 929 Greener, J. G., Kandathil, S. M., Moffat, L., & Jones, D. T. (2022). A guide to
930 machine learning for biologists. *Nature Reviews Molecular Cell Biology*, *23*(1),
931 40–55.
- 932 Greenwell, B. (2021). fastshap: Fast approximate shapley values [Computer software
933 manual]. Retrieved from <https://CRAN.R-project.org/package=fastshap>
934 (R package version 0.0.7)
- 935 He, H., & Garcia, E. A. (2009). Learning from imbalanced data. *IEEE Trans-
936 actions on Knowledge and Data Engineering*, *21*(9), 1263-1284. doi: 10.1109/
937 TKDE.2008.239
- 938 Hemes, S., Desbois, G., Urai, J. L., Schröppel, B., & Schwarz, J.-O. (2015). Multi-
939 scale characterization of porosity in boom clay (hades-level, mol, belgium)
940 using a combination of x-ray μ -ct, 2d bib-sem and fib-sem tomography. *Micro-
941 porous and mesoporous materials*, *208*, 1–20.
- 942 Immerkær, J. (1996). Fast noise variance estimation. *Computer Vision
943 and Image Understanding*, *64*(2), 300-302. Retrieved from [https://
944 www.sciencedirect.com/science/article/pii/S1077314296900600](https://www.sciencedirect.com/science/article/pii/S1077314296900600) doi:
945 <https://doi.org/10.1006/cviu.1996.0060>
- 946 James, G., Witten, D., Hastie, T., Tibshirani, R., James, G., Witten, D., ... Tibshi-
947 rani, R. (2021). Statistical learning. *An introduction to statistical learning:
948 with applications in R*, 15–57.
- 949 Jayachandran, I. S. A. J. (2023). *Replication data for: An object-based approach to
950 differentiate pores and microfractures in petrographic analysis using explain-
951 able, supervised machine learning* [dataset]. Harvard Dataverse. Retrieved
952 from [https://dataverse.harvard.edu/dataset.xhtml?persistentId=doi:
953 10.7910/DVN/T2LESU](https://dataverse.harvard.edu/dataset.xhtml?persistentId=doi:10.7910/DVN/T2LESU) doi: doi:10.7910/DVN/T2LESU
- 954 John, C. R. (2020). Mlevel: Machine learning model evaluation [Computer software
955 manual]. Retrieved from <https://CRAN.R-project.org/package=Mlevel> (R
956 package version 0.3)
- 957 Jolliffe, I. T., & Cadima, J. (2016). Principal component analysis: a review and
958 recent developments. *Philosophical transactions of the royal society A: Mathe-
959 matical, Physical and Engineering Sciences*, *374*(2065), 20150202.
- 960 Kassambara, A., & Mundt, F. (2020). factoextra: Extract and visualize the results
961 of multivariate data analyses [Computer software manual]. Retrieved from
962 <https://CRAN.R-project.org/package=factoextra> (R package version
963 1.0.7)
- 964 Kuhn, M. (2022). caret: Classification and regression training [Computer software
965 manual]. Retrieved from <https://CRAN.R-project.org/package=caret> (R

- 966 package version 6.0-93)
- 967 Kuhn, M., & Johnson, K. (2019). *Feature engineering and selection: A practical ap-*
 968 *proach for predictive models*. Chapman and Hall/CRC.
- 969 Kuhn, M., Johnson, K., et al. (2013). *Applied predictive modeling* (Vol. 26).
 970 Springer.
- 971 Kuhn, M., & Silge, J. (2022). *Tidy modeling with r*. ” O’Reilly Media, Inc.”.
- 972 Lê, S., Josse, J., & Husson, F. (2008). FactoMineR: A package for multivariate anal-
 973 ysis. *Journal of Statistical Software*, *25*(1), 1–18. doi: 10.18637/jss.v025.i01
- 974 Lee, D., Karadimitriou, N., Ruf, M., & Steeb, H. (2021). Detecting micro fractures
 975 with x-ray computed tomography. *arXiv preprint arXiv:2103.12821*.
- 976 Legland, D., Arganda-Carreras, I., & Andrey, P. (2016). Morpholibj: integrated li-
 977 brary and plugins for mathematical morphology with imagej. *Bioinformatics*,
 978 *32*(22), 3532–3534.
- 979 Li, B., Tan, X., Wang, F., Lian, P., Gao, W., & Li, Y. (2017). Fracture and vug
 980 characterization and carbonate rock type automatic classification using x-ray
 981 ct images. *Journal of Petroleum Science and Engineering*, *153*, 88–96.
- 982 Loncaric, S. (1998). A survey of shape analysis techniques. *Pattern recognition*,
 983 *31*(8), 983–1001.
- 984 Lucia, F. J. (1983, 03). Petrophysical Parameters Estimated From Visual De-
 985 scriptions of Carbonate Rocks: A Field Classification of Carbonate Pore
 986 Space. *Journal of Petroleum Technology*, *35*(03), 629-637. Retrieved from
 987 <https://doi.org/10.2118/10073-PA> doi: 10.2118/10073-PA
- 988 Lucia, F. J. (1995, 09). Rock-Fabric/Petrophysical Classification of Carbonate
 989 Pore Space for Reservoir Characterization1. *AAPG Bulletin*, *79*(9), 1275-
 990 1300. Retrieved from [https://doi.org/10.1306/7834D4A4-1721-11D7-](https://doi.org/10.1306/7834D4A4-1721-11D7-8645000102C1865D)
 991 [8645000102C1865D](https://doi.org/10.1306/7834D4A4-1721-11D7-8645000102C1865D) doi: 10.1306/7834D4A4-1721-11D7-8645000102C1865D
- 992 Lundberg, S. M., & Lee, S.-I. (2017). A unified approach to interpreting model pre-
 993 dictions. *Advances in neural information processing systems*, *30*.
- 994 Lønøy, A. (2006, 09). Making sense of carbonate pore systems. *AAPG Bulletin*,
 995 *90*(9), 1381-1405. Retrieved from <https://doi.org/10.1306/03130605104>
 996 doi: 10.1306/03130605104
- 997 Mayer, M. (2023). shapviz: Shap visualizations [Computer software manual]. Re-
 998 trieved from <https://CRAN.R-project.org/package=shapviz> (R package
 999 version 0.5.0)
- 1000 McCreesh, C. A., Ehrlich, R., & Crabtree, S. J. (1991). Petrography and reservoir
 1001 physics ii: relating thin section porosity to capillary pressure, the association
 1002 between pore types and throat size. *AAPG bulletin*, *75*(10), 1563–1578.
- 1003 Młynarczuk, M., Górszczyk, A., & Ślipek, B. (2013). The application of pattern
 1004 recognition in the automatic classification of microscopic rock images. *Comput-*
 1005 *ers & Geosciences*, *60*, 126–133.
- 1006 Mollajan, A., Ghiasi-Freez, J., & Memarian, H. (2016). Improving pore type iden-
 1007 tification from thin section images using an integrated fuzzy fusion of multiple
 1008 classifiers. *Journal of Natural Gas Science and Engineering*, *31*, 396–404.
- 1009 Mulchrone, K. F., & Choudhury, K. R. (2004). Fitting an ellipse to an arbitrary
 1010 shape: implications for strain analysis. *Journal of structural Geology*, *26*(1),
 1011 143–153.
- 1012 Murphy, K. P. (2022). *Probabilistic machine learning: an introduction*. MIT press.
- 1013 Neal, F. B., & Russ, J. C. (2012). *Measuring shape*. CRC Press.
- 1014 Norbistrath, J. H., Eberli, G. P., Laurich, B., Desbois, G., Weger, R. J., & Urai, J. L.
 1015 (2015). Electrical and fluid flow properties of carbonate microporosity types
 1016 from multiscale digital image analysis and mercury injection. *AAPG bulletin*,
 1017 *99*(11), 2077–2098.
- 1018 R Core Team. (2022). R: A language and environment for statistical computing
 1019 [Computer software manual]. Vienna, Austria. Retrieved from [https://www.R-](https://www.R-project.org/)
 1020 [project.org/](https://www.R-project.org/)

- 1021 Rabbani, A., Fernando, A., Shams, R., Singh, A., Mostaghimi, P., & Babaei, M.
 1022 (2021). Review of data science trends and issues in porous media research
 1023 with a focus on image-based techniques. *Water Resources Research*, 57(10),
 1024 e2020WR029472.
- 1025 Schloerke, B., Cook, D., Larmarange, J., Briatte, F., Marbach, M., Thoen, E., ...
 1026 Crowley, J. (2021). Ggally: Extension to 'ggplot2' [Computer software man-
 1027 ual]. Retrieved from <https://CRAN.R-project.org/package=GGally> (R
 1028 package version 2.1.2)
- 1029 Schubert, E., Sander, J., Ester, M., Kriegel, H. P., & Xu, X. (2017). Dbscan revis-
 1030 ited, revisited: why and how you should (still) use dbscan. *ACM Transactions*
 1031 *on Database Systems (TODS)*, 42(3), 1–21.
- 1032 Seers, T. D., & Hodgetts, D. (2014). Comparison of digital outcrop and conven-
 1033 tional data collection approaches for the characterization of naturally fractured
 1034 reservoir analogues. *Geological Society, London, Special Publications*, 374(1),
 1035 51–77.
- 1036 Seers, T. D., & Hodgetts, D. (2016). Extraction of three-dimensional fracture trace
 1037 maps from calibrated image sequences. *Geosphere*, 12(4), 1323–1340.
- 1038 Shapley, L. S. (1953). Stochastic games. *Proceedings of the national academy of sci-*
 1039 *ences*, 39(10), 1095–1100.
- 1040 Sharifi, J. (2022). Multi-pore rock physics model: An intelligent approach for car-
 1041 bonate rocks. *Journal of Petroleum Science and Engineering*, 218, 111002.
 1042 Retrieved from [https://www.sciencedirect.com/science/article/pii/](https://www.sciencedirect.com/science/article/pii/S092041052200852X)
 1043 [S092041052200852X](https://doi.org/10.1016/j.petrol.2022.111002) doi: <https://doi.org/10.1016/j.petrol.2022.111002>
- 1044 Singh, A., Rabbani, A., Regenauer-Lieb, K., Armstrong, R. T., & Mostaghimi, P.
 1045 (2021). Computer vision and unsupervised machine learning for pore-scale
 1046 structural analysis of fractured porous media. *Advances in Water Resources*,
 1047 147, 103801.
- 1048 Skalinski, M., & Kenter, J. A. M. (2015). Carbonate petrophysical rock typing:
 1049 integrating geological attributes and petrophysical properties while linking
 1050 with dynamic behaviour. *Geological Society, London, Special Publications*,
 1051 406(1), 229–259. Retrieved from [https://www.lyellcollection.org/doi/](https://www.lyellcollection.org/doi/abs/10.1144/SP406.6)
 1052 [abs/10.1144/SP406.6](https://doi.org/10.1144/SP406.6) doi: 10.1144/SP406.6
- 1053 Stafford, I., Kellermann, M., Mossotto, E., Beattie, R. M., MacArthur, B. D., & En-
 1054 nis, S. (2020). A systematic review of the applications of artificial intelligence
 1055 and machine learning in autoimmune diseases. *NPJ digital medicine*, 3(1), 30.
- 1056 Sun, Y., Wong, A. K., & Kamel, M. S. (2009). Classification of imbalanced data: A
 1057 review. *International journal of pattern recognition and artificial intelligence*,
 1058 23(04), 687–719.
- 1059 Tang, Y., Horikoshi, M., & Li, W. (2016). ggfortify: unified interface to visualize
 1060 statistical results of popular r packages. *R J.*, 8(2), 474.
- 1061 Thrun, M. C. (2018). *Projection-based clustering through self-organization and*
 1062 *swarm intelligence: combining cluster analysis with the visualization of high-*
 1063 *dimensional data*. Springer.
- 1064 Thrun, M. C., & Ultsch, A. (2021). Using projection-based clustering to find
 1065 distance-and density-based clusters in high-dimensional data. *Journal of Clas-*
 1066 *sification*, 38, 280–312.
- 1067 Urbanowicz, R. J., Suri, P., Cui, Y., Moore, J. H., Ruth, K., Stolzenberg-Solomon,
 1068 R., & Lynch, S. M. (2020). A rigorous machine learning analysis pipeline
 1069 for biomedical binary classification: application in pancreatic cancer nested
 1070 case-control studies with implications for bias assessments. *arXiv preprint*
 1071 *arXiv:2008.12829*.
- 1072 Van Der Maaten, L., Postma, E. O., van den Herik, H. J., et al. (2009). Dimension-
 1073 ality reduction: A comparative review. *Journal of Machine Learning Research*,
 1074 10(66–71), 13.
- 1075 Venables, W. N., & Ripley, B. D. (2002). *Modern applied statistics with s* (Fourth

- 1076 ed.). New York: Springer. Retrieved from [https://www.stats.ox.ac.uk/](https://www.stats.ox.ac.uk/pub/MASS4/)
 1077 [pub/MASS4/](https://www.stats.ox.ac.uk/pub/MASS4/) (ISBN 0-387-95457-0)
- 1078 Vogelstein, J. T., Bridgeford, E. W., Tang, M., Zheng, D., Douville, C., Burns, R., &
 1079 Maggioni, M. (2021). Supervised dimensionality reduction for big data. *Nature*
 1080 *communications*, *12*(1), 2872.
- 1081 Wang, A. Y.-T., Murdock, R. J., Kauwe, S. K., Oliynyk, A. O., Gurlo, A., Brgoch,
 1082 J., ... Sparks, T. D. (2020). Machine learning for materials scientists: An
 1083 introductory guide toward best practices. *Chemistry of Materials*, *32*(12),
 1084 4954-4965.
- 1085 Wang, Z., Ge, H., Zhou, W., Wei, Y., Wang, B., Liu, S., ... Du, S. (2022). Char-
 1086 acterization of pores and microfractures in tight conglomerate reservoirs. *Inter-*
 1087 *national Journal of Hydrogen Energy*, *47*(63), 26901-26914.
- 1088 Weger, R. J. (2006). *Quantitative pore/rock type parameters in carbonates and their*
 1089 *relationship to velocity deviations*. University of Miami.
- 1090 Weger, R. J., Eberli, G. P., Baechle, G. T., Massafello, J. L., & Sun, Y.-F. (2009).
 1091 Quantification of pore structure and its effect on sonic velocity and permeabil-
 1092 ity in carbonates. *AAPG bulletin*, *93*(10), 1297-1317.
- 1093 Weihs, C., Ligges, U., Luebke, K., & Raabe, N. (2005). klar analyzing german busi-
 1094 ness cycles. In D. Baier, R. Decker, & L. Schmidt-Thieme (Eds.), *Data analy-*
 1095 *sis and decision support* (p. 335-343). Berlin: Springer-Verlag.
- 1096 Wickham, H. (2007). Reshaping data with the reshape package. *Journal of Statisti-*
 1097 *cal Software*, *21*(12), 1-20. Retrieved from [http://www.jstatsoft.org/v21/](http://www.jstatsoft.org/v21/i12/)
 1098 [i12/](http://www.jstatsoft.org/v21/i12/)
- 1099 Wickham, H. (2016). *ggplot2: Elegant graphics for data analysis*. Springer-Verlag
 1100 New York. Retrieved from <https://ggplot2.tidyverse.org>
- 1101 Wickham, H., Averick, M., Bryan, J., Chang, W., McGowan, L. D., François, R.,
 1102 ... Yutani, H. (2019). Welcome to the tidyverse. *Journal of Open Source*
 1103 *Software*, *4*(43), 1686. doi: 10.21105/joss.01686